Gundula Teichert, BSc.

Cellulose based blend thin films - preparation, characterization and surface interactions with proteins

MASTER'S THESIS

to achieve the university degree of

Diplom-Ingenieurin

Master's degree programme: Advanced Materials Science

submitted to

Graz University of Technology

Supervisor

Assoc.Prof. Mag.rer.nat. Dr.rer.nat. Stefan Spirk

Institute of Paper, Pulp and Fibre Technology

Graz, September 2019

AFFIDAVIT

I declare that I have authored this thesis independently, that I have not used other than the declared sources/resources, and that I have explicitly indicated all material which has been quoted either literally or by content from the sources used. The text document uploaded to TUGRAZonline is identical to the present master's thesis.

_____   _____

Date   Signature

Danksagung

Als ich mich dafür entschied meine Masterarbeit bei Prof. Spirk im Bereich der biobasierten Kunststoffe schreiben zu wollen, konnte ich noch nicht ahnen welch aufregende Zeit auf mich zukommen würde.

Besonderer Dank geht an Prof. Stefan Spirk für die Ermöglichung dieser Arbeit, die Chance Erfahrungen auf Tagungen und Konferenzen zu sammeln und die Betreuung der Masterarbeit. Des weitern möchte ich mich beim Institut für Papier, Zellstoff und Fasertechnik für die Unterstützung bedanken.

Im Rahmen der Arbeit war ein 7-wöchigen Auslandsaufenthalt in Göteborg bei Prof. Nypelö an der Chalmers University möglich. Ich möchte mich nicht nur bei der TU Graz für die finanzielle Unterstützung durch das Stipendium Research Abroad bedanken, sondern vor allem bei Tiina Nypelö für die Einladung nach Schweden. Neben der Möglichkeit eine Vielzahl von Messgeräten kennen zu lernen, war es eine unvergessliche Erfahrung die Kultur und die tollen Bedingungen an der Uni zu erleben. Thank you for all your support during my master thesis!

Die Arbeitsgruppe in Österreich darf aber auch nicht unerwähnt bleiben – danke euch allen für die stehts freundschaftlich, hilfsbereite Arbeitsatmosphäre. Danke Kati für die Einschulung am SPR, Werner die allgegenwärtige Unterstützung, Krissi, Carina und Steffi (meinen liebsten Munchkins) für unzählige Stunden, Gespräche und Austausch; ich bin dankbar euch an meiner Seite zu haben.

Danke an Caterina Czibula von der Rastersondenmikroskopie-Arbeitsgruppe an der Montanuniversität Leoben für die Hilfe mit den AFM-Auswertungen und die zur Verfügungstellung der Reibungskraftmessungen (FFM).

Bei meiner Familie und Freunden möchte ich mich für all die Bestärkungen und Unterstützung in allen Lebenslagen, während des gesamten Studiums bedanken, die mir diese Studentenzeit erst ermöglicht haben.

Abstract

Cellulose thin films have been extensively studied as biobased model surfaces since the turn of the millennium. Cellulosic surfaces show very low interaction with proteins, due to the high degree of solvation in aqueous systems. A modification with functionalized cellulose derivatives is of upcoming interest for biosensor development.

In this thesis the protein interactions with cellulose substituted with hydrophobic residues blended with amorphous cellulose were examined. A blend system of the cellulose precursor – trimethylsilyl cellulose (TMSC) with hydroxypropyl stearate cellulose (HPCE) was manufactured in different mixing ratios by spin coating and regenerated via vaporous hydrochloric acid. Through spin coating the mixture of polymers in common solution phase separate and lead to various morphologies, depending on the polymer ratio, spin coating conditions and polymer properties, such as polarity and molecular weight.

Thin films from HPCE in two degrees of substitution (DS 1 and DS 3) with TMSC were characterized by multiple surface sensitive techniques: attenuated total reflection infrared spectroscopy, wettability estimation, profilometer and atomic force microscopy. Protein interaction was determined with bovine serum albumin as a probe using label free monitoring techniques such as surface plasmon resonance spectroscopy (SPR) and quartz crystal microbalance with dissipation (QCM-D).

Kurzfassung

Seit der Jahrtausendwende werden Zellulosedünnschichtfilme umfangreich in Hinblick auf biobasierte Modeloberflächen untersucht. Zelluloseoberflächen sind in wässrigen Systemen hoch assoziiert mit Wassermolekülen und daher in der Interaktion mit Proteinen gehemmt. Eine Modifizierung mit funktionalisierten Zellulosederivaten wird von immer größerem Interesse für die Entwicklung von Biosensoren.

In der vorliegenden Arbeit wurden Proteininteraktionen mit Blendsystemen aus hydrophoben Zellulosederivaten und amorpher Zellulose, untersucht. Blendfilme aus dem Zelluloseausgangsstoff Trimethylsilylzellulose (TMSC) und hydropoxypropyl stereatylester Zellullose (HPCE) wurde in verschiedenen Mischverhältnissen durch Spincoating hergestellt und in salzsaurer Atmosphäre regeneriert. Abhängig vom Polymermischungsverhältnis, den Polymermaterialeigenschaften, wie deren Polarität und Molekülgewicht und den Bedingungen beim Spincoaten kommt es beim Spincoaten zur Phasenseparation der Polymermischung aus dem gemeinsamen Lösungsmittel und führt zu unterschiedlichen Morphologien.

Zwei Blendsysteme aus HPCE in unterschiedlichen Substitionsstufen (DS 1 und DS 3) jeweils mit TMSC wurden mittels vielfältiger oberflächensensitiver Techniken charakterisiert: Abgeschwächte Totalreflexion Infrarotspektroskopie, Benetzbarkeitsmessung, Profilometer und Raster Kraft Mikroskopie. Die Oberflächeninteraktionen mit Proteinen wurden durch Experimente mit Rinderserumalbumin als einem gängigem Proteinmarker bestimmt, detektiert durch labelfreie Messmethoden wie Oberflächenplasmonenresonanzspektroskopie (SPR) und Quarzkristall-Microwaage mit Schwingungsdämpfung (QCM-D).

Table of Content

1. Aims and Motivation

The present master thesis aims at the investigation of several surface interactions of cellulose based blend thin films. Based on the intriguing study on trimethyl silyl cellulose (TMSC) as a cellulose precursor with cellulose stearyl ester (CSE) blends in protein adsorption another aliphatic tailored cellulose derivative was chosen for further investigation with bovine serum albumin (BSA). Solutions of immiscible polymers phase separate while spin coating, resulting in patterned thin films, depending on the polymer properties, the mixing ratio, spinning conditions, etc. Hydroxy propyl cellulose (HPC) with different degrees of substitution (DS) of stearyl esters (DS 1 and DS 3) is blended with TMSC. According to transient bilayer theory various morphologies are expected in the spin coated films and therefor tunable surface interactions with BSA.

Thin films of TMSC with hydroxypropylstearate cellulose (HPCE) (DS 1 and DS 3 respectively) blended in a common solvent are manufactured in three ratios and are characterized before and after regeneration of TMSC using the following methods. The neat films are put in relation to the properties of the blend films.

- Attenuated total reflection infrared spectroscopy (ATR-IR) for tracking the conversion of TMSC to regenerated cellulose.
- Profilometer for film thickness
- Contact angle (CA) measurement for determining the wettability of water and diiomethan and further calculating the surface free energy
- Atomic force microscopy (AFM) for depicting the surface topography
- Surface plasmon resonance (SPR) spectroscopy for label free BSA monitoring
- Quartz crystal microbalance with dissipation (QCM-D) for BSA monitory with viscoelastic properties as well for water exchange experiments for water amount in thin films

A basic understanding of HPCEs in TMSC blend systems and the according regenerated films in terms of phase separation, non-specific protein interaction as well as water uptake is to achieve.

2. Introduction

2.1. Cellulose

As stiff fibers in wood cell walls, cellulose is the most abundant polymer on earth. Together with hemicellulose and lignin molecules as matrix materials the linear β-1,4 linked D-glucose molecules of cellulose determine the extraordinary mechanical properties of wood at light weight. [1] In the cotton plant, cellulose occurs naturally in rather pure form without any combination with lignin or polysaccharides. Same as bacterial cellulose, which is produced extracellularly by e.g. Acetobacter xylinum strains is from research interest. Other natural resources besides trees are annual plants like wheat straw or bamboo, marine creatures (tunicates), algae, and bacteria. [2,3]

Chemical structure

Cellulose fundamental substructure is the most abundant monosaccharide D-glucose, which are linearly connected as anhydroglucose unit (AGU) in cellulose from wood 10 000. All hydroxy groups in cellulose are in equatorial position and therefore it is thermodynamically the most stable configuration of glucose subunits In nature, cellulose occurs mainly in crystalline form, the metastable cellulose I phase. Multiple cellulose chains are stacked parallel, with respect to the reducing end forming elementary fibrils, that further aggregate into larger microfibrils, with a diameter 5-50 nm and several micrometers in length. [4] By regeneration or mercerization the chains are rearranged, with hydrogen bonds between cellulose chains pointing the reducing end in antiparallel. The most stable cellulose II conformation is achieved. [2,4] Further polymorph cellulose III is reached by ammonia treatment and subsequent heat treatment of cellulose I and II. [5]

Solubility of cellulose

The tight network of hydrogen bonds results in hygroscopic and hydrophilic features within the macromolecule, due to the staged ring structures and the spatial proximity of the hydroxy groups. This explains why the macromolecule cellulose does not dissolve in water but swell, due to partial insertion of solvent molecules. [3] Available solvents for cellulose are exotic, often toxic and reactive. Aqueous solvents often contain transition metal complexes, like cupric hydroxide with aqueous ammonia (Cuam), cupriethylenediamine hydroxide (Cuen), or tri(ethylenediamine) cadmium

hydroxide (Cadoxen). For non-aqueous solvents are unicomponent and multicomponent systems are known, high ionic strength is in common for all. E.g. N-methylmorpholine-N-oxide (NMMO), ionic liquids or multicomponent systems such as dimethylacetamide with lithium chloride (DMAc–LiCl) and dimethyl sulfoxide with tetrabutylammoniumfluoride trihydrate (DMSO–TBAF). In industrial applications like the Lyocell process N-methylmorpholine-N-oxide (NMMO) is still very popular, while the others solvents are used in laboratory.[6]

2.2. Cellulose Derivatives

Cellulose is insoluble to most of the common solvents and hence cellulose needs to be derivatized, if solution is targeted to use for film formation. The substitution or partial substitution of the hydroxyl groups is the useful approach that leads to solubility of the cellulose derivative. Charged substituents such as carboxymethyl groups in carboxymethyl cellulose (CMC) promote water solubility, the insertion of hydrophobic groups achieves the solubility to organic solvents. Solubility behavior of macromolecules in general depends on molecular weight, polarity and the molecule shape. For various cellulose derivatives the solubility is decreasing again at very high degree of substitution (DS). [7]

2.2.1. Trimethylsilyl cellulose (TMSC)

Trimethylsilyl cellulose (TMSC) is a hydrophobic derivative of cellulose and synthesized by a homogeneous reaction of cellulose dissolved in ammonia with hexamethyldisilazane (HMDS) at enhanced pressure in an autoclave leaving ammonia as side product. For partial silylated TMSC less HMDS is used than the stoichiometric amount. For very low DS it is hydrolytic desilylated in THF/ammonia using saccharin as a catalyst, whereby the synthesis becomes a heterogenous reaction, caused by the solubility window of DS 1.6 – 2.6 TMSC in THF for linters cellulose. [7,8]

TMSC with high DS (> 2) is a hairy-rod macromolecule dissolves in toluene or chloroform and can be used for preparation of single component cellulose films as well as for blend films. [9–13]

Exposing the TMSC to HCl it is desilylated, volatile hexamethyl disiloxane segregates into the gas phase and regenerated cellulose remains. In this context the bulky hairy-rod macromolecules are compressed into a compact cellulose network, which is tightly bond via H-bridges. [14,15] Further regenerations methods via a (nano) focused

electron beam for nanostructured cellulose films [16], via UV-light when a photoacid generator is added for photolithography [17]. Spin coated thin films are mainly amorphous after regeneration. [18]

2.2.2. Hydroxypropyl stearate cellulose (HPCE)

Hydroxypropyl stearate cellulose is a hydroxypropyl cellulose derivate with stearoyl chloride Derivatization of hydroxypropyl cellulose with different chain length of fatty acid chlorides in various degree of substitution (DS) modifies the hydrophobicity as well as solubility of the molecule and the glass transition temperature/melting point. A comprehensive study considering kinetics and reaffirming reproduceable methods have been published by Nau et al. (2018). [19]

Figure 1 Chemical structure of hydroxy propyl cellulose (HPC), cellulose stearyl ester (CSE) and hydroxypropyl stearate cellulose (HPCE)

Commercially available hydroxy propyl cellulose (HPC) is esterified with stearate chlorides, exploiting the good solubility in a wide range of organic solvent of HPC. Therefore, the synthesis of HPCE is easier manageable than of cellulose stearoyl ester (CSE). The reaction of HPC with stearic acid chloride was implemented in THF at 80°C, while for CSE DS 3 cellulose is dissolve in DMAc/LiCl and need to react for 1 h, while stirring at 100°C.

With short chain HPCE (C4) derivatives mesophasic behavior is observable and blends of different DS were found to arrange in in thermotropic cholesteric mesophase, with iridescent colors at room temperature. [20] Nanoparticle coatings of HPCE (C18) DS 3, lead to superhydrophobic surfaces, which can switched by thermal annealing above the melting temperature, demonstrating interesting potential uses for example as stimuli-responsive barrier coatings. [19]

2.3. Cellulose thin films

Cellulose thin films have not only been interesting for the modelling approach of complex materials from renewable resources, which are further process in different variety of all-day life products from paper to textiles, but also recently interaction studies. [21]

Thin films refer to films that have a thickness in nanometer to the micrometer range. This allows their utilization in surface sensitive techniques that are based on observing change in film thickness and conformation, such as surface plasmon resonance (SPR) and quartz crystal microbalance with dissipation monitoring (QCM-D). Cellulose thin films have been used for observing adsorption phenomena and water interactions and used as a model for system utilizing cellulose fibers or other cellulosic material. [15]

Thin films can be prepared either from solution or dispersion, given that the dimension of the particulate matter in the matter are minute enough to allow nanometer film thickness. Spin coating and Langmuir-Blodgett (LB) deposition techniques are mostly applied. [15,21]

2.3.1. Spin coating of thin films

Spin coating was found to be a simple method to manufacture uniform thin films from solution up to 30 µm thickness. By tuning spinning parameters (acceleration, speed and surrounding temperature) and solution parameters (polymer and solvent properties, concentration, viscosity and solvent volatility), it is simple and easy to manufacture thin films with various thickness. A solid support material is set on a rotary plate and fixed with an attached vacuum pump. In static spin coating the sufficient amount solution of two polymers in a common solvent is deposit on the surface to cover it and the spinning program is started immediately afterwards. Spinning off the main part of the solution a thin film remains and dries due to evaporation of the solvent. [14][22] A mixture of (partly) immiscible macromolecules in a common leads to phase separation while spin coating, establishing a simple method for manifold patterned thin films. [23]

2.3.2. Films from cellulose in suspensions

One product one comes across in everyday life is paper. Wood is digested to pulp, hence delignificated either via the sulfite or sulfate process, is bleached and afterwards pressed to sheets [4] For thin films colloidal nanocellulose dispersions e.g., cellulose

nanocrystals (CNCs), cellulose nanofibers (CNFs) can be spin coated with subsequent mild heat treatment for stable ultra-thin films of few nanometers with high crystallinity. [21] CNCs are established by sulfuric acid hydrolysis of the semicrystalline fractions in the microfibrils, leaving the crystallites. In contrast CNFs are obtained by strong mechanical shearing of fibers assisted through an oxidizing pretreatment, for example catalyzed with 2,2,6,6-tetramethylpiperidine-1-oxyl. [24] A crucial point of stable films is to prevent re-dispersion and gel formation; therefore, the heat treatment for removing water from the crystals and electrostatics brought in via functionalized crystals are common approaches. Further ionic surfaces are used as precoatings. While spin coating the anisotropic nano cellulose is not aligned and tuning of the film thickness is limited especially for CNFs, due to gel formation even at low concentration (1w%). [21]

2.3.3. Films from cellulose solutions

Solvents for cellulose have been described above and can be used for thin film formation. Thin films from N-methylmorpholine-N-oxide (NMMO) with water, (DMAc) with LiCl or urea with aqueous NaOH are known. Like mentioned above these solvents are expensive and toxic. The resulting thin films can be tuned in thickness and mainly amorphous. [21]

2.3.4. Films from cellulose derivatives

Spin coating of dissoluted cellulose derivatives with subsequent regeneration leads to amorphous cellulose thin films. [18] One exception is cellulose carbamate, where regeneration can be implemented while spin coating, when coated from alkaline aqueous solution. [25] Several precursors for cellulose are known: As described before TMSC is regenerated by vaporous HCl. (see Chapter 2.2.1) Cellulose xanthate thin films is also regenerated by vaporous HCl, with disadvantage of formation of solid NaCl, which needs get rinsed off. [26] Cellulose acetate is able to be regenerated by ammonia vapor from aqueous NH_4OH. [21]

2.3.5. **Mechanism of micro phase separation**

Based on thermodynamics, mixtures of two polymers in a common solvent tend to segregate and lead to enrichment of the polymers in separated phases. In the present thesis, biopolymer mixtures were spin coated in different mixing ratios and the phase separation of the resulting blend thin film was verified by atomic force microscopy (AFM).

A two-component (A, B) system is designed by the change of Gibbs free enthalpy on mixing ΔG_{mix}, given through the enthalpy change of mixing ΔH_{mix}, the absolute temperature T and the entropy change on mixing ΔS_{mix} (Equation (1)). High molecular weight molecules show a small positive entropy change through dissolution. Therefore, the enthalpy has a decisive impact. [27]

$$\Delta G_{mix} = \Delta H_{mix} - T\Delta S_{mix} \tag{1}$$

If $\Delta G_{mix} > 0$, the mixture is not separated, while for $\Delta G_{mix} < 0$ decomposition appears. For polymer mixtures, Flory-Huggins lattice theory was developed, considering the conformation entropy of polymer macromolecules and intermolecular interactions. The free enthalpy for binary mixtures is given by the molar volume (n_a, n_b; according to the different polymers a, b) and volume fraction Φ_a and $\Phi_b = 1 - \Phi_a$ for the second polymer, consequently. [27]

$$\Delta G_{mix} = RT \left(n_a ln\Phi_a + n_b \ln(1 - \Phi_a) + \chi \, (1 - \Phi_a) \right) \tag{2}$$

X is the Flory-Huggins' interaction parameter and is a function of the mole fraction, the temperature, and the degree of polymerization. [27,28] To determine the change of mixing enthalpy ΔH_{mix} Hildebrand and Hansen discovered solubility parameters. Hildebrand's approach is to consider the cohesive energy, where all intermolecular forces are eliminated. Hansen approached three types of molecular interactions: Non polar dispersive interactions caused by constantly morphing of negatively charged electron clouds. Permanent dipole-dipole interactions contribute polar cohesive forces. and finally the highest proportion, H-bondings. [28] Dissolving the polymer in several solvents with different Hansen-solubility parameters, provides information about the interaction of the analyte with the solvent and allows to conclude to phase separation behavior. [29]

In the case of spin coating blend thin films, the evaporation of the solvent is accelerated, and a thin film remains on the support. [22] With light/neutron reflectivity or time-resolved, small-angle X-ray scattering during spin coating the formation of phase structures can be directly studied. In this manner it was suggested, that through the energy impact of spinning the polymer mixture arrange itself spontaneously in a bilayer, with a clear interface. [30,31] Spin coating of a mixture of two polymer solutions in a common solvent (i), first leads to removal of most of the solution (ii) and then to vertical stratification (iii), where the more polar molecules reassemble on the hydrolyzed silicon or gold support and the other polymer on top of it. (Figure 2) By evaporation of the solvent a concentration gradient is caused within the bilayer arrangement. Due to interfacial instabilities the layers start to break up, and dewetting leads to a lateral phase separation, as a consequence of complex interplay of rapid film thinning and subsequently decreasing mobility. [31]

At the interface between the support surface, the dissolution of polymer mixture and the atmospheric environment several factors affect the non-equilibrium process of spin coating. Several other mechanisms rule the pattern of micro phase separation, like dewetting mechanisms of the polymer dissolutions and to the support surface and nucleation growth of the polymer segregations.
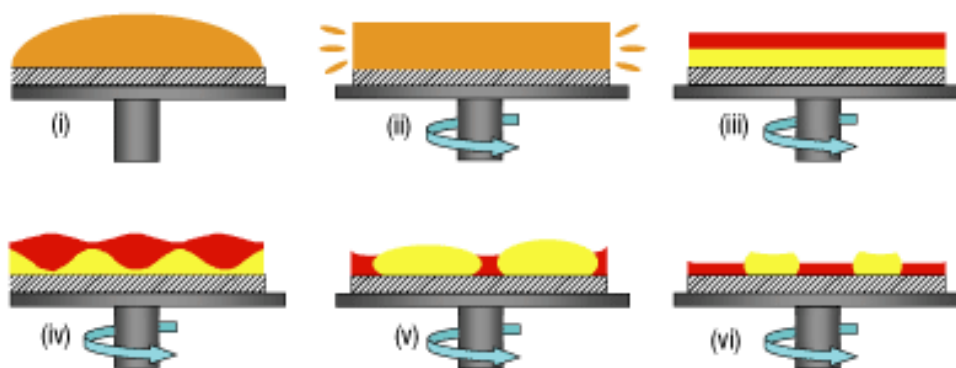

Figure 2 From Heriot (2005) [31]: Transient bilayer theory: Both polymers are resolved in a common solvent (i). Spinning off most of the dissolution (ii) cause the remaining polymers to arrange in a bilayer. (iii) Through evaporation of the solvent, the interface starts to destabilize (iv) and the laterally phase separation is provoked (v), till the solvent is evaporated (vi).

First simplified, the effect of dewetting of thin films has been studied on a polystyrene thin film on a silicon support. Annealing the film above its glass transition temperature leads to dewetting, and the smooth film breaks up and cylindrical holes appear. With growth of the holes, rims appear ahead of them, which eventually start to contact each other and decay into droplets. (Figure 3) [32,33]
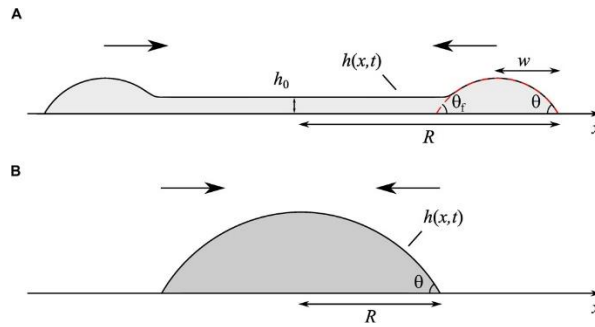
Figure 3 (A) Scheme of dewetting film in cross-sectional profile. Rims with certain width (w) and contact angle θ are connected by a thin film of thickness h_0 in an angle $θ_f$. (B) Final equilibrium dewetting droplet. [33]

For investigation of phase separation in blend thin films, the consideration is extended to liquid/liquid dewetting observation, where partial wetting with a finite contact angle is considered on a liquid substrate, representing immiscible interfaces in a bilayer arrangement. In macroscopic films holes open to minimize the surface free energy as a result of gravimetrical force balance of capillary driving force and hydrodynamic losses and are filled by the polymer from the lower layer. (Figure 4) In contrast, for thin films long range forces as interfacial tensions and surface tensions need to be taken in account. Considering the bilayer system as a stratified system two fundamental modes are expected. The transverse bending mode is described by a vertical displacement and is ruled by surface tensions. Longitudinal peristaltic mode and is enhanced with capillary waves in the film thickness. [34]
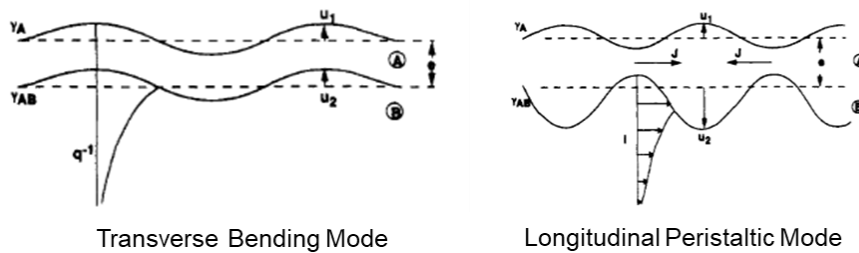

Transverse Bending Mode   Longitudinal Peristaltic Mode

Figure 4 Liquid-liquid dewetting: fundamental modes of stratified liquids [34]

If these droplet fluctuations reach a critical size, where the surface term of the emerged nucleus with big curved surface is exceeded by the stability of the new stable phase in enough volume, domains evolve, which are enriched in one polymer. Although the local segregated areas reach a local equilibrium, smaller droplets tend to shrink and dissolve again, due to diffusion from high-curvature droplets to low-curvature droplets in terms to reduce interfacial free energy. This coarsening of the system is called Oswald ripening. [35]

Since these mechanisms are highly dependent on diffusive mass transport, the variation of film thickness influences the lateral phase separation. Based on smaller vertical distances in thin films, the pattern tends to coarsen in thinner films. [23,36] The film thickness can be tuned by the spin coating parameters and is influenced by the dissolution viscosity, the vapor pressure of the solvent and the surface wettability. [22]

Strong interactions between the lower bilayer and the support surface dominate the phase segregation in thin films and stabilize the bilayers. A breakup of the upper layer as well as dewetting of the lower one is less likely, which can lead to a thin film with stratified domains. [23,32,37]

Circumstances in the surrounding atmosphere such as varying temperature and relative humidity, can accelerate the solvent evaporation, and lead to cylindrical break ups in the thin film, or to condensed humidity, which can adhere on the support surface or in the spinning solution and hinder the film formation. Even if this hypothetical dewetting leading to pore formation is based on similar physical principles, it is spatially and chronologically different to the dewetting during phase separation. [30,37,38] System parameters and mechanism on interfaces are summarized in Figure 5.
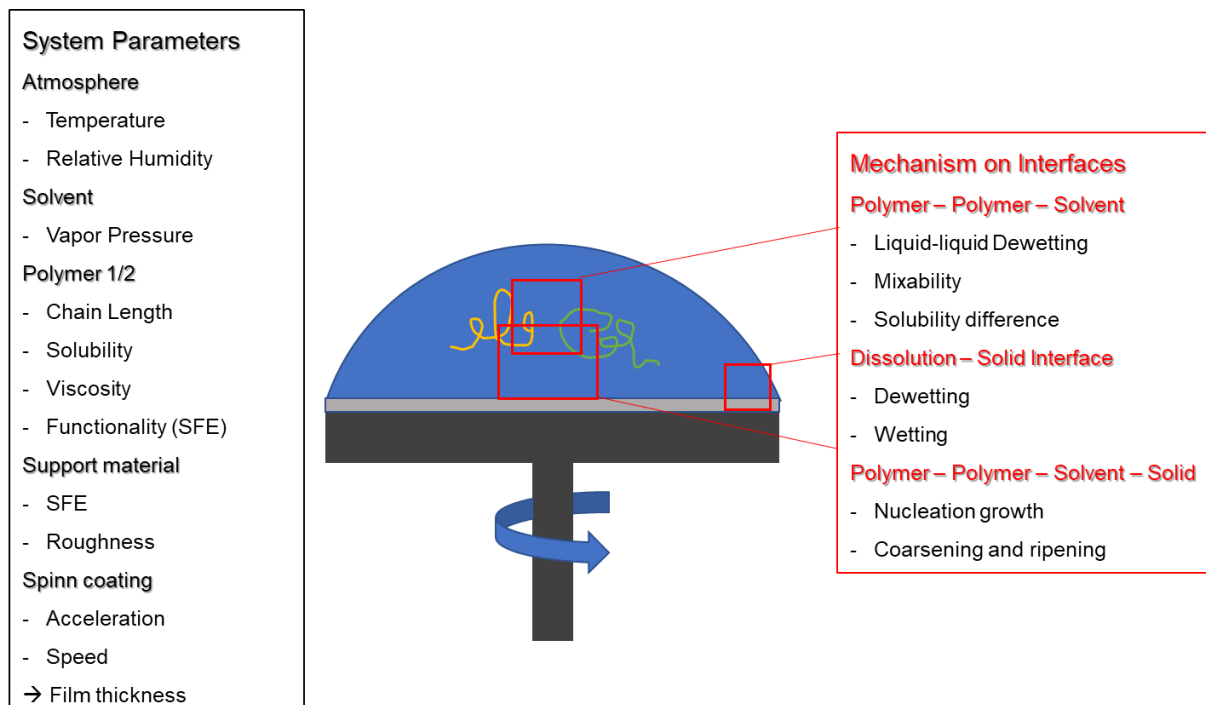

Figure 5 Schematic representation of the parameters, which influence micro phase separation.

2.3.6. Blend polymer thin films

Synthetic Polymer based Blend Systems

With the aim to understand phase separation behavior and the resulting patterns, the study of synthetic polymer blend systems is of keen interest. Polymethylmethacrylate (PMMA) and polystyrene (PS) are immiscible polymers, available with a narrow chain length distribution. Therefore, PMMA and PS are a well tunable system for various requirements in research set ups.

Walheim et al. investigated mixture of polystyrene (PS) and polymethylmethacrylate (PMMA) that was spin coated from three different solvents (toluene, THF, and methyl ethyl ketone, MEK) on to three different support materials (silicon oxide SiO_x, gold (Au) and an organic monolayer (ODM)). While in thin films spin coated from toluene and THF on an Au-Surface, PMMA is evaluated over a PS background, the pattern dramatically changes when produced from a MEK dissolution. Toluene and THF are better solvents for PS than for PMMA. Therefore, the solvent is evaporated first in the PMMA enriched phase, while the PS- enriched domains are still present in a swollen state, which collapse with further vaporization. For MEK the case is vice versa, and PS domains are finally elevated. According to the transitive bilayer theory, PMMA is found to be the lower layer on polar support material (like SiO_x and hydrolyzed Au) with PS domains on top spin coated from THF. On a highly hydrophobic support, like a ODM-covered surface, PS is arranged on the solid interface and PMMA an almost continuous layer on top with several cylindrical holes filled with PS from below. [23]

Deuterated polystyrene (PS) and polymethylmethacrylate (PMMA) with different molecular weight was mixed and examined by neutron reflectivity. The results suggest that the highly nonpolar polystyrene forms a well-defined phase-separated bilayer structure on top of the PMMA enriched layer. Higher molecular weight affected the phase separation trough a broader interface while spin coating, probably based on reduced mobility of bigger molecules in the solvent. [30]

Further, examinations of PS/PMMA blends were done with same polymer ratio, but varying film thickness, adjusted by different spin coating parameter. It was shown, that the structure is a coarsened, the thinner the film was manufactured. [23,36]

Biopolymer Blend Systems with TMSC as a Cellulose Precursor

According to the transient bilayer theory on TMSC/PS blends, the highly non-polar polystyrene forms the layer on the atmosphere interface, spin coating from toluene dissolution on silicon a support. This results in thin films with disk like PS agglomeration embedded in the TMSC matrix. By regeneration, the received cellulose is shrunk in volume. Hence, the circular PS domains are further enhanced from the cellulose matrix and the roughness increases. With this strategy the hydrophobicity of surfaces is tunable depending on the mixing ratio. In contrast to the situation in TMSC/PMMA blends the TMSC arranges the upper bilayer and dewets to disk-like droplets in the PMMA matrix. Due to the better solubility of TMSC in toluene, these domains remain subsequently swollen and finally collapse beneath the PMMA matrix level. Regeneration leads to deeper cavities with cellulose on the bottom and around them. [39–41]

An extensive study on blends with TMSC and cellulose triacetate (CTA) at different humidity showed that the concept of transient bilayer theory is capable for TMSC based blends with some limitations. Increasing humidity while spin coating enhances the pore growth. Condensed water droplets from the ambient air cool the solvent during evaporation, nucleate, grow and sink into the polymer solution and form breath structures. By washing off the CTA phase it turned out that mainly the CTA was affected by humidity. Certain domain size in the blends further triggered breath structures, which is the case in the 2:1 ratio. Further pores were related to humidity induced dewetting with rim formation. Exclusive water droplets in CTA indicate that TMSC builds the lower phase during vertical stratification, although its SFE is lower than of CTA, which is discussed as an enhanced affinity between Si in TMSC and in the Si-wafer. Another feature in TMSC/CTA blends is layer inversion. A thin TMSC overlayer is merging over the hole blend film, which was indicated by water CA measurements. Since TMSC is better soluble in chloroform it remains more fluid and mobile while solvent evaporation. Therefor the viscose CTA penetrates the TMSC phase during dewetting and TMSC partly merges onto the air-polymer interface. [38] These effects are less prone to synthetic, hydrophobic polymers and expand further aspects to biopolymer-based blend systems.

The concept of microphase separated thin films has further extended to TMSC and lignin palmitate (LP) blends resulting in lignocellulosic amphiphilic biocomponent films.

Quite smooth thin films with roughness values of 1 – 10 nm were presented. In 1:3 ratio a comparable thicker LP layer dewets, but does not form the continuous matrix, either leads to formation of lignin palmitate cavities. The diameter of the LP cavities increases from 1:3 – 3:1 ratio from ~ 150 nm to ~ 600 nm. The domains in all mixing fractions are very homogeneous with the extraordinary morphology in 1:1 ratio which is very reminiscent to honeycombs in a cellulose matrix. [11]

The blend system of TMSC with poly-3-hydroxybutyrate (PHB) formed morphologies similar to TMSC/PMMA for ratio TMSC:PHB 1:10, - 1:1. In both systems TMSC droplets contract in circular droplets, however in this case they protrude over the PHB matrix, which is in contrast to TMSC/PMMA films. [12]

Like in the present thesis the blend of TMSC : cellulose stearoyl ester (CSE) uses also fatty acid derivative of cellulose - a hairy-rod molecule. Compared to the other TMSC based blends rather large domains occur. Depending of the mixing ratio either the CSE phase or the TMSC contracts in droplets of ~ 500 nm. The chloroform washed cellulose : CSE film in 1:1 ratio showed underlying cellulose domains which are overlapped by CSE. [13]

Besides the HCl vapor regeneration step further possibilities for surface modifications of TMSC based blends are possible. Due to the insolubility of the regenerated cellulose in the common apolar solvent, the second, non-converted phase can be washed off selectively and patterned cellulose is left behind. Further cellulase an enzyme from e.g. trichoderma viride fungus can be used to remove specific the cellulose. [42] Depending on the second component potentially another route might happen to be possible. Poly-3-hydroxybutyrate is degradable by PHB depolymerase. [12] CTA is selectively regeneratable to cellulose, by exposure to ammonia vapor. Therefore, a further opportunity is accessible for patterned cellulose films by hydrolyzing either one or the other cellulose derivative. [21,38]

2.3.7. Surface analysis of blend systems by Atomic Force Microscopy

Atomic force microscopy (AFM) enables non-destructive height measurements of surfaces in the range of several nm up to 1 µm with lateral resolution in the nanometer range. [43] Since microphase separation in thin films results in a height difference - due to a mechanism of lateral phase separation and dewetting - AFM is a suitable measurement method to study microphase separated thin films.

Simply put, by scanning a fine AFM tip line by line across a surface by means of a piezoelectric actuator, the topography of the surface is detected (Figure 6). The tip is fixed at the end of a flexible beam, the cantilever with defined spring constant. When a laser beam is focused to the back of the cantilever, it is reflected towards photodetector, and the position of the reflected beam on the detector provides information of the z-value of the topography. The sample itself is mounted on a piezo scanner, where through a feedback loop x,y,z coordinates are recorded. This mechanical, non-optical approach does not need any optical or magnetic lenses, can be carried out under atmospheric conditions and requires no elaborate inert or vacuum conditions. Therefore, AFM is especially dedicated for surface analysis including biopolymer films. [44]
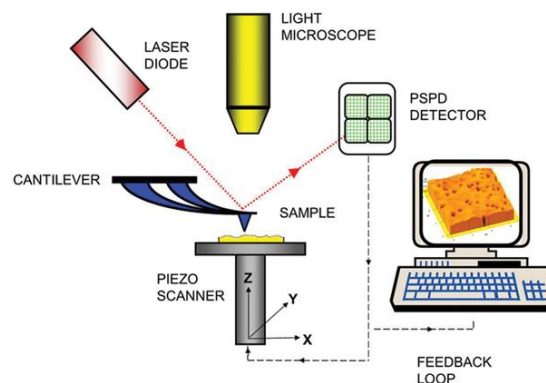

Figure 6 Scheme of the AFM measurement set up [45]

Bringing the tip in proximity to the surface, they interact on an atomic level with each other. Attractive forces are based on Van der Waals interactions that increase to the power of 6 with decreasing distance. Repulsive forces are originating from ionic or Pauli exclusion. These are short-range force proportional to the power of 12 of distance. The sum of both relations is reproduced by the Lenard-Jones Potential. (Figure 7) Approaching the tip, the attractive forces predominate first. In this distance, *non-contact AFM* is implemented. Hovering a probe over the surface (5 -10 nm), the cantilever is deflected according to the topography of the sample. Therefore, it is a

non-destructive method with negligible friction force, but with low lateral and z-resolution. Conversely, in *contact AFM* the tip constantly touches the surface during scanning. Lateral (friction) forces act on the sample, which might scratch the ample surface or cause wear of the tip. In *dynamic tapping mode,* the cantilever-tip system is excited to oscillate close to its resonant frequency. While tapping, the tip is constantly running through repulsive and attractive interactions. At fixed frequency, the amplitude is used as feedback parameter to image the topography. Electric charges at the surface affect the interaction and the energy dissipation of the cantilever. [46,47]
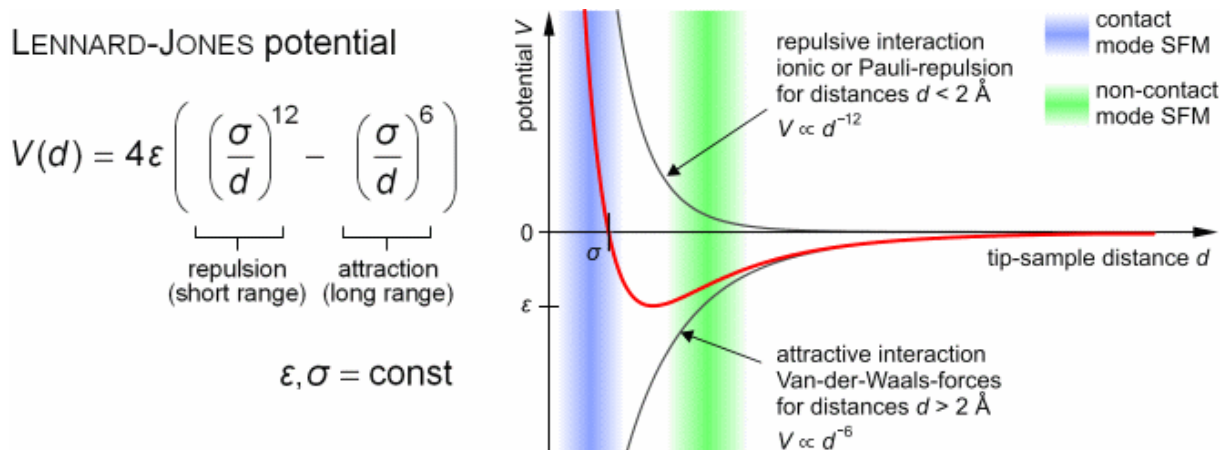
LENNARD-JONES potential

$$V(d) = 4\varepsilon \left(\left(\frac{\sigma}{d} \right)^{12} - \left(\frac{\sigma}{d} \right)^{6} \right)$$

repulsion (short range)   attraction (long range)

$\varepsilon, \sigma = const$

potential V

repulsive interaction
ionic or Pauli-repulsion
for distances $d < 2$ Å
$V \propto d^{-12}$

contact mode SFM

non-contact mode SFM

0

σ

tip-sample distance d

ε

attractive interaction
Van-der-Waals-forces
for distances $d > 2$ Å
$V \propto d^{-6}$

Figure 7 Lenard-Jones Potential in Scanning Force Microscopy (Figure by Steve Pawlizak, 2009.) [48]

Since in contact mode the AFM tip is approached straight to the surface, the radius and the opening angle of the tip influence the topography data. Sharp edges may be mapped with a smaller slope to the plateau. Therefore protrusion appear bigger and cavities smaller, according to the tip fineness. [49]

Revealing information beyond topography

Recording in tapping mode operation the phase shift and amplitude change of the driving system with respect to the resulting cantilever oscillation, a phase contrast image can be created. It reveals differences of viscoelasticity, adhesion, and contact area within the specimen. Thus, stiff materials appear dark (higher phase shift) and soft materials bright (lower phase shift) in the image. [44]

2.4. Surface interactions on thin films adsorption of biomolecules

Part of interface phenomena between biomolecules and thin film surface are common adsorption events, which are influenced by properties of the surface, the biomolecule functionality and some external parameters. [50]

This thesis focuses on protein interactions with cellulose derivative blend thin films, using the transport protein bovine serum albumin (BSA). Proteins are polypeptides build of L-amino acids and the amino acid sequence is called primary structure (Figure 8). The amino acids can be classified by their residues: charged, non-polar and polar residues. Based on the sequence the functional groups are interacting with each other, building intramolecular H-bonds and either coil up to α-helices or fold up to β-sheets, connected by so-called loop elements. A three-dimensional structure - the secondary structure - is formed. The long-range order of these elements forms the tertiary structure. The polypeptide chain is densely folded and shows specific shape, like globular or rod form, with active sites depending on the task of the protein.[51,52]
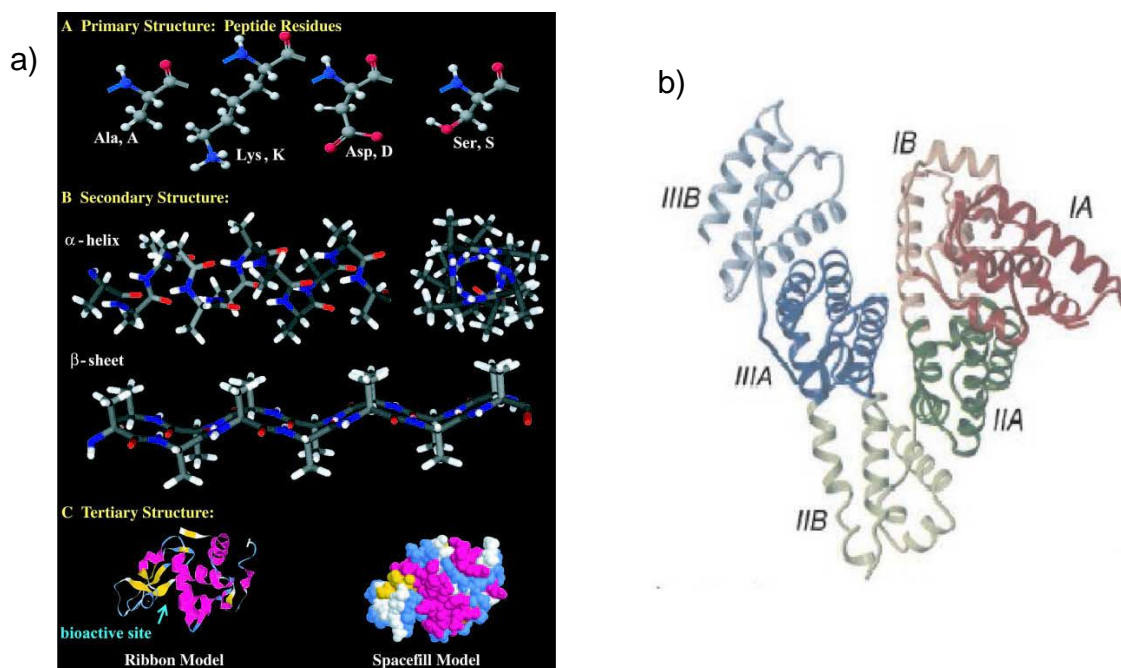

Figure 8 (a) Description of primary, secondary (with α-helix and β-sheet) and tertiary structure of polypeptides i.e. proteins [52],(b) ribbon model of bovine serum albumin [53]

Functionality of Bovine Serum Albumin (BSA)

BSA is the most abundant protein in blood serum of a cow and has various active sites both for polar and less polar compounds. It can interact with water, metal ions (eg. Ca^{2+}, Zn^{2+}, Cu^{2+}) hormones, fatty acids and so on. Due to the extensive transport properties of BSA it controls many physiological functions like stabilizing the pH value and the osmotic pressure of the blood. Based on this extensive functionality it is very prone for non-specific adsorption and is used as a blocking reagent in adsorption experiments, when specific protein-ligand interactions are the objective. (Figure 9) [54]

BSA is often chosen as a model substance for several research objectives. Especially in the highly topical fields of study like tissue biomaterial interactions and biomedical implants, protein interactions play a key factor. Protein agglomeration can lead to thrombosis, but also is essential for proper vascularization. [55]
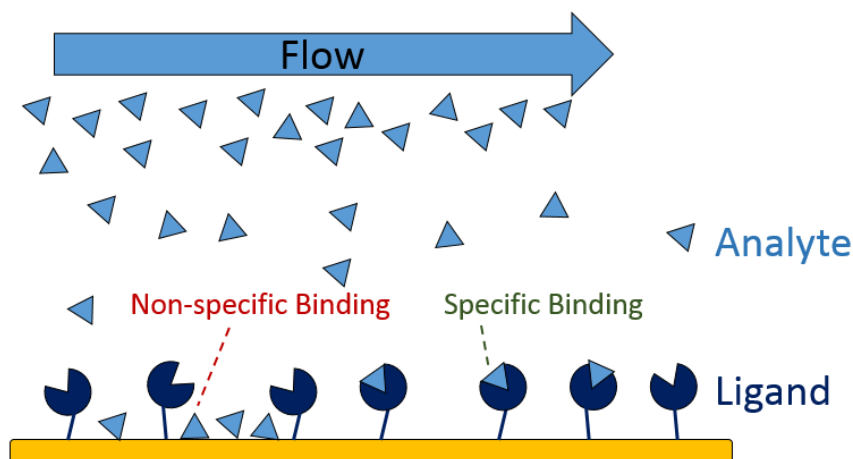

Figure 9 Schematic overview of non-specific and specific binding of analyte (protein) and ligand [56]

Due to the complex structure and functionality of proteins they do not act like small, rigid particles. Simple attach and detachment events from an interface are less likely for biomolecules and possible structural re-arrangements and changing surface affinities need to be taken in account. Conformation of proteins are influenced by temperature, pH value and ionic strength and do change within adsorption and desorption events. At certain high ionic strength proteins denature, due to a reduced availability of solvent molecules, which are more likely to solvate the ions. With rising temperature first H-bonds get destroyed and the denaturation of the protein structure occurs. [50,57]

Table 1 Properties of proteins that affect their interaction with surfaces. [58]

Property	Effect
Size	Larger molecules can have more sites of contact with the surface
Charge	Molecules near their isoelectric point generally adsorb more readily
Structure Stability	Less stable proteins, such as those having less intramolecular cross-linking, can unfold to a greater extent and form more contact points with the surface
Unfolding rate	Molecules that rapidly unfold can form contacts with the surface more quickly

Charged amino acids of proteins in aqueous solutions are located to the outside of the protein, due to better solvation and therefore possibly interact with the surfaces. Based on the protonation and deprotonation depending on the pK_a value of the functional groups in the amino acids, the conformation of the protein changes with pH and forms different amount of contacts to the surface. For the reason of extended contact area bigger molecules are more likely to adsorb and more hindered to desorb again. The isoelectric point identifies the pH value where the charge over the whole molecule exhibits zero. At the IP solubility reaches a minimum and intermolecular electric repulsion is reduced. Therefore more interactions with the surface are possible and more proteins are likely to adsorb. [58,59]

BSA is a globular, heart shaped transport protein with an isoelectric point (*pI*) at pH 4.7. Hydrodynamically it was described already in the 70ties as a prolate ellipsoid with the dimensions of 140*40*40 $Å^3$, determined by calculation out of several hydrodynamic properties for example sedimentation dependence on ionic strength and transient electric birefringence. [60,61] The three-dimensional structure of BSA is determined by using cross-linking reagents and performing mass spectrometry. By modifying BSA with lysine specific cross-linkers and quantifying with tandem mass spectrometry the distances between lysine residues are resolved. With complementary data from various cross-linkers and assistance of O-18 labeling the tertiary structure of BSA is obtained. [53]

The conformation of BSA may change in an event of adsorption. As shown by Norde et al. (1999) [62] with circular dichroism spectroscopy the α-helix fraction is reduced, and the β-turn content is increased after monomolecular displacement from

hydrophobic polystyrene particles, while BSA regains the native secondary structure after desorption from hydrophilic silica surface. The change in secondary structure affects the thermal stability and lowers enthalpy of denaturation of the protein. [62]

Besides protein conformation and its surface charges protein-surface interactions are also influenced by surface characters – see an overview in Table 2. The surface functionalities are reflected in parameters like surface energy, charge, polarity, wettability and morphology, and influence the adhesion to proteins. Essentially all surfaces carry electrically charged groups in aqueous solution, due to dissociation/association or specific adsorption of ions from solution. Contrary charges of the surface and the protein promote adsorption, which is further affected by the topography and texture of the surface. A surface texture fitting to the protein shape enhances the interaction area and therefore the adhesion energy. Wettability of the surface, reflected in the surface free energy value, states the hydration of the interface and therefor represents the accessibility for adsorbates. Hydrophobic surfaces are less hydrated and therefore the balance of adsorption Gibbs free energy is more exergonic compared to hydrophilic surfaces in aqueous solution, where the adsorption is hindered through hydration, which needs to be replaced with the adsorbate. Proteins as adsorbate are amphiphilic and there are indications that maximum affinity occurs on intermediate polar surface and on heterogenic surfaces with varying surface energetics. [58,59,63,64]

Table 2 Influence of surface properties on protein adsorption [58]

Feature	Effect
Topography	Greater texture exposes more surface area for interaction with proteins
Composition	Chemical makeup of a surface will determine the types of intermolecular forces governing interaction with proteins
Hydrophobicity	Hydrophobic surfaces tend to bind more protein
Heterogeneity	Nonuniformity of surface characteristics results in domains that can interact differently with proteins
Potential	Surface potential will influence the distribution of ions in solution and interaction with proteins

2.4.1. Established Techniques for the Study of Protein Adsorption

Studying protein interactions with surfaces several aspects of adsorption are of interest, such as kinetics, thickness of the protein layer, identity and conformation of adsorbed proteins, structure of the adsorbed protein layer, and/or the types of forces operating between the protein and the surface. With respect of the chemical composition spectroscopic and spectrometric methods have been established like auger electron spectroscopy, X-ray photoelectron spectroscopy, ATR-IR or secondary ion mass spectroscopy [55]

Topography analysis by AFM gives the opportunity to monitor the BSA adsorption amount ex situ. Therefor the surface must be enough smooth, so that the BSA molecules with a size of 140 x 40 x 40 $\mathring{A}^3$ are protruded on the surface. [65] Using fluorescently labeled BSA the adsorbed amount can be established by fluorescence scanning of the fluorescence intensity [59]

For real time monitoring of protein adsorption on thin film surfaces, the challenge is to set up a very accurate measurement system for small amounts in the nanogram range, which is detectable with a reasonable time resolution. One of the oldest techniques to study protein adsorption in real-time is the enzyme-linked immunosorbent assay (ELISA), where antibodies are used to detect specific interactions to the proteins, providing information about the adsorbed quantity. Another possibility is to use the inverse piezoelectric effect in a quartz crystal microbalance (QCM) and determine gravimetrically the adsorbed mass due to the frequency change. An optical method to study adsorption phenomena on thin films is described by surface plasmon resonance spectroscopy (SPR). Plasmon resonance on a gold surface is highly sensitive on structural and chemical changes of the thin film and shows an accordant angle shift of the minimum in the spectrum based on changes of the systems refractive index. Another optical method is ellipsometry where polarized light is used to determine the thickness of the adsorbed protein layer. [55,66,67]

3.5.1.1.SPR - Surface plasmon resonance

In an interaction of light with matter at an interface between a prism and a metal thin film, surface plasmons occur due to a phenomenon of attenuated total reflection, whereby the free metal electron gas gets excited to a highly delocalized status. In measurements set up according to Kretschmann, a monochromatic laser beam is led thorough a prism, which is properly attached to gold thin film of the SPR sensor slide via an elastomeric film, with fitting refractive index. The SPR sensor is mounted with the glass side backwards to the prism. (Figure 10) Surface plasmon resonance is caused in the metal thin film and effected by the attached analyte thin film and the bulk liquid flow behind it, as described in detail below. [68,69]
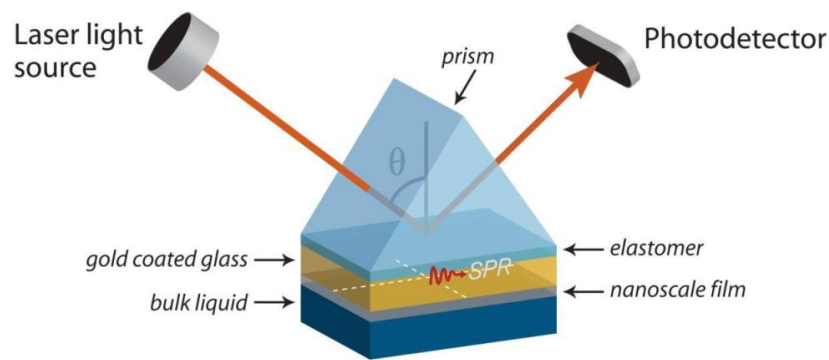
Figure 10 Schematic overview of surface plasmon resonance in SPR measurement set up in Kretschmann configuration [70]

Light refraction in general occurs on the transition of two translucent materials and is described by Snell's law.

$$n_1 \sin \theta_1 = n_2 \sin \theta_2 \qquad (3)$$

Where n is the refractive index for material 1 and material 2, respectively, θ_1 the angle of the incident beam and θ_2 the angle of the outgoing beam. If light refraction from medium with high refractive index to medium with low refractive index ($n_1 > n_2$) takes place, the angle of the outgoing beam is bigger than the angle of the incoming beam. Increasing the angle of incident at critical conditions total internal reflection occurs and the beam proceeds along the interface (Figure 11 d). Increasing the angle further, the beam is not entering the second medium anymore, but is reflected in the same angle instead (Figure 11e). Since light is considered an electromagnetic wave, based on Maxwell equation it can't change its propagation direction in one point. Instead a standing wave on the surface is emerged, which is entering the less dens material in form as an exponentially decaying wave and therefore an evanescent field accrues. (Figure 12)
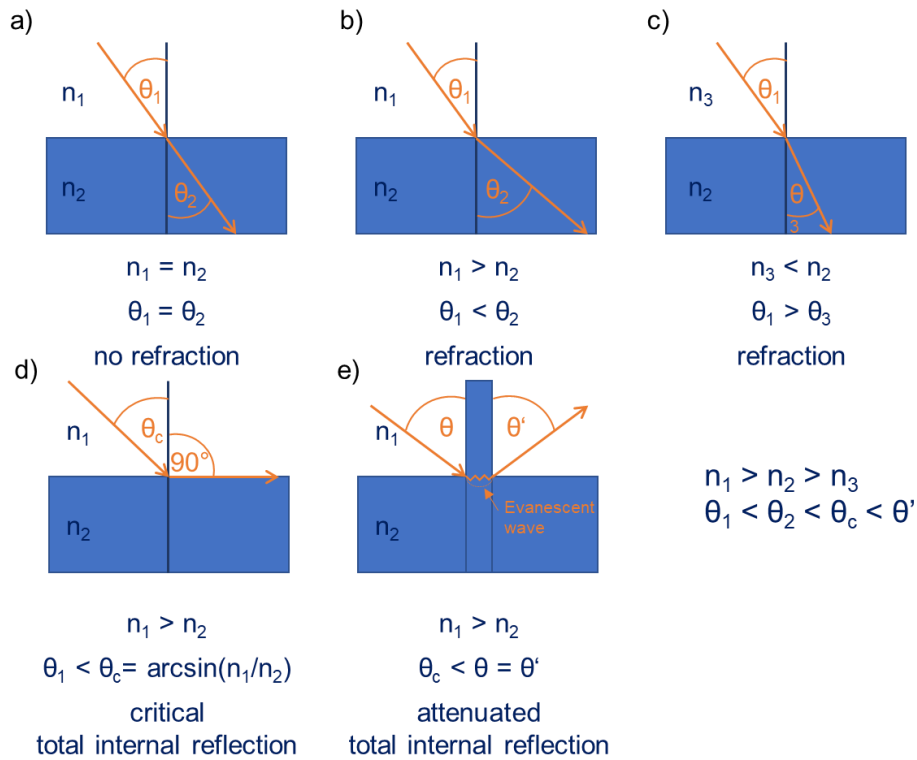
a)

n_1 θ_1

n_2 θ_2

$n_1 = n_2$

$\theta_1 = \theta_2$

no refraction

b)

n_1 θ_1

n_2 θ_2

$n_1 > n_2$

$\theta_1 < \theta_2$

refraction

c)

n_3 θ_1

n_2 θ_3

$n_3 < n_2$

$\theta_1 > \theta_3$

refraction

d)

n_1 θ_c 90°

n_2

$n_1 > n_2$

$\theta_1 < \theta_c = \arcsin(n_1/n_2)$

critical

total internal reflection

e)

n_1 θ θ'

n_2 Evanescent wave

$n_1 > n_2$

$\theta_c < \theta = \theta'$

attenuated

total internal reflection

$n_1 > n_2 > n_3$

$\theta_1 < \theta_2 < \theta_c < \theta'$

Figure 11 Depiction of Snell's law: (a) $n_1 = n_2$, no reflection (b) transition from high optical density to lo low density (c) vice versa (d) critical total internal reflection (e) attenuated total internal reflection with later shift.

If the evanescent field fits the free electron oscillation of the metal, surface plasmons resonance occurs on the metal surface along the interface to the dielectric thin film. The evanescent field of the surface plasmon wave decays into the thin film and is highly sensitive to refractive index of the sample. [68,71]
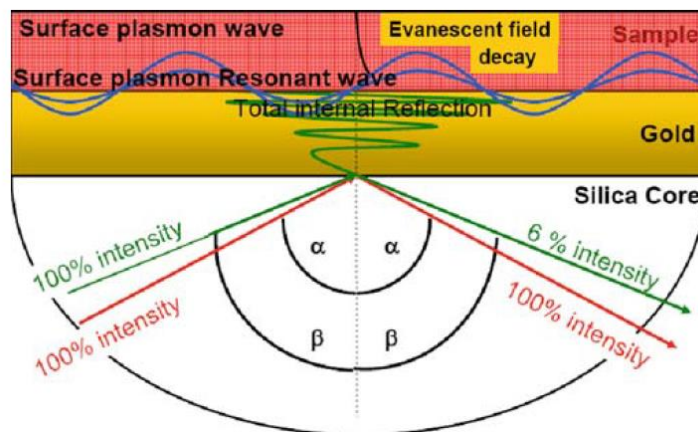
Figure 12 From [68] Schematic depiction of surface plasmon resonance conditions. Surface plasmon resonance occur for laser with certain wavelength (green) in angle of incidence α. In this attenuated total internal reflection, an evanescent field is caused, which implies surface plasmon waves (blue). Under critical conditions in angle of incident β 100% of the light are reflected. (red)

In resonant angle all conditions are fulfilled for surface plasmon resonance, where the reflectance of the incident light changes significantly. By varying the incident beam

angle and detecting the intensity of the reflected light SPR spectra can be plotted. At plasmon resonance conditions the plot show a sharp minimum down to ~6% of the laser intensity.(Figure 12) [69] In Figure 13 characteristics of a SPR spectrum are represented. In point 3 total internal reflection (TIR) occurs and the light is almost fully reflected. The position of the peak minimum is determined by the intersection point of the steepest falling slope and maximum rising slope. At point 2 the according minimum intensity is recorded. [72]
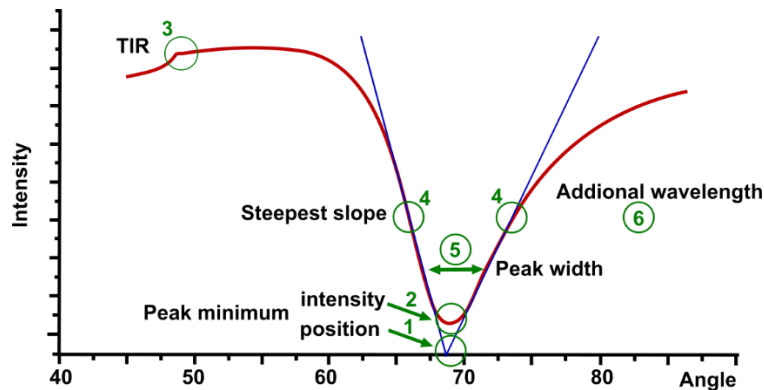
Figure 13 Important points in a characteristic curve of a MP-SPR-spectrum [73]

Using two lasers with different wavelength it is possible to estimate the film thickness and the according refractive index via multi-layer modelling. Therefor one of the SPR curves is shift by the value of the chromatic dispersion Δn/Δλ and the thickness is determined through intersection point of the SPR spectra. The chromatic dispersion is determined in advance by measuring the system in two different solvents – the so-called 2-color-approach. An approach for multilayer density analysis of cellulose thin films has just been published recently. Bionavis developed an according software called layer-solver. [74,75]

Signal to mass calculation

De Feijter et al. developed an equation for calculating the adsorbed mass from the angular shift of the peak minimum without modelling. It is dependent of the angular response of the plasmon resonance peak Δθ and the refractive index increment (dn/dc) of the adsorbing layer.

$$\Gamma_p = \frac{\Delta\Theta * k * d_p}{dn/dc} \tag{4}$$

k * dp can be considered as constant for thin layer smaller than 100nm and is dependent on the sensor type, the measurement set up and wavelength of the laser.

2.4.1.2. QCM-D – Quartz Crystal Microbalance with Dissipation Monitoring

For QCM-D measurements, a quartz crystal is mounted in a temperature-controlled flow chamber attached to a peristaltic pump. The chamber connects to the gold electrodes of the quartz crystal, and they get excited to oscillate in its matching resonance frequency by applying alternating voltage. Hence, a standing wave is generated in the edge of the crystal additional to several overtones. In the 'ring down' mode, the external driving force is turned off and the oscillation is left to decay freely. Whereas in this context the voltage is generated in the quartz crystal due to the cyclical deformation of the piezoelectric material, where top and bottom surface move tangentially in an antiparallel fashion. This set-up leads to two resulting parameters: the acoustic resonance frequency and the dissipation, resulting from the exponential decay from the oscillation. Dissipation reflects the loss of energy per oscillation period divided by the total energy stored in the system and thereby contains additional information on mechanical properties like viscosity, density, and elasticity. In further consequence it reveals changes in film morphology like swelling or cross-linkage, and the shear modulus of the film can be modeled. [66]

Derived by Sauerbrey, the resonance frequency is in linear relation to changes in the resonator mass for rigid films. Hence QCM-D is an extremely sensitive mass balance for nanogram to microgram level changes in mass per unit area, due to the highly accurate measurability of frequencies.

$$\Delta f_n = \frac{n}{C} * m_f = -\frac{n}{C} \rho_f h_f \qquad \rightarrow \qquad \Delta m = -C * \frac{1}{n} \Delta f_n \qquad (5)$$

where n is the overtone, m_f the areal mass density of the adsorbed film (mass per unit area), finally ρ_f and h_f are the density and the thickness of the film. The mass sensitivity constant C is -0.177 mg·m^{-2}·Hz^{-1} for crystals with fundamental resonance frequency of 5 MHz. Suggested by Tammelin et al. it is possible to assume the density for cellulose thin films as 1200 kg·m^{-3} and calculate the film thickness according to the formula (6) [76]

$$h = \frac{\Delta m_{Sauerbrey}}{\rho_{assumed}} \qquad (6)$$

The Sauerbrey equation does not take into account dissipation and is only valid, when the adsorbed mass is evenly distributed, rigid without any slip and small compared to the mass of the crystal itself. [77–79] However, swelling cellulose films are flexible molecular systems and show viscoelastic properties, which cause dissipation of

oscillation energy due to mechanical losses in the flexible mass and is reflected in the dissipation measurement. Voigt modeling is taking dissipation in account by fitting both the dissipation and frequency data. This model describes the viscoelastic layer on the crystal with a spring analogy, whereas the properties are split into a viscous dashpot and an elastic spring and further fitted both in parallel. With the known physical properties of the QCM-D-crystal (density and thickness) and the bulk liquid (with its physical properties like viscosity, density, angular frequency of oscillation and the penetration depth of the shear wave) and the adsorbed layer, which is defined by its density, shear elasticity, viscosity and thickness the layers can be fitted using Δf and ΔD from at least two overtones. [79,80]

An alternative is to compare frequency shifts due to adsorbed layers of different harmonics to derivate the shear compliance shown by Johannsmann (2001). By plotting the normalized frequency shift versus the squared order of overtone the linear relationship and the y-intercept gives the effective mass, with coupled solvent. [81]

Water content determined by exchange of water with deuterium

Using the density difference of H_2O (ρH_2O) and its deuterated derivative D_2O (ρD_2O), the exchangeable water content in thin films can be studied, caused by a change of mass at same amount coupled water. Therefore, the films are held under constant flow till a stable baseline is reached and the films are in an equilibrium, swollen status. The difference of the frequency shift caused by the exchange with D_2O of a bare crystal $(\frac{\Delta f_n}{n})_{bare}$ and a swollen film $(\frac{\Delta f_n}{n})_{film}$ is put in ratio with the densities of ρH_2O (0.9982 g·cm^{-3} at 20°C) and ρD_2O (1.1050 g·cm^{-3} at 20°C) – see Equation (7). [82]
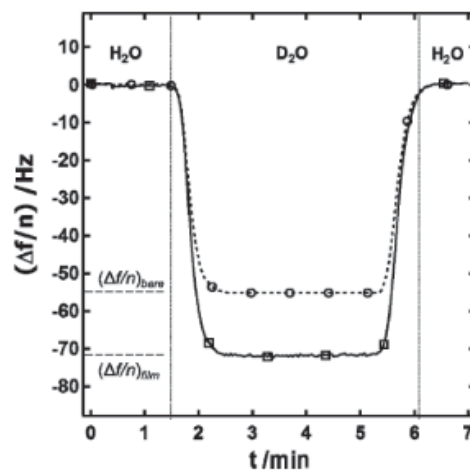

Figure 14 From [82] Schematic representation of a water exchange experiment. Squares for a bare gold sensor and circles for a film.

$$\left(\frac{\Delta f}{n}\right)_{Water} = \frac{\left(\frac{\Delta f_n}{n}\right)_{film} - \left(\frac{\Delta f_n}{n}\right)_{bare}}{\left(\frac{\rho D_2 O}{\rho H_2 O}\right) - 1} \qquad (7)$$

The Sauerbrey relation allows the calculation of the exchanged water mass Γ_{Water} in mg·m^{-2} in same principle as in (5).

$$\Gamma_{Water} = -C \left(\frac{\Delta f_n}{n}\right)_{Water} \qquad (8)$$

Finally, the water content is represented in percent, by putting the water mass in context with the film mass in air.

$$\% water\ content = \frac{\left(\frac{\Delta f_n}{n}\right)_{Water}}{\left(\frac{\Delta f_n}{n}\right)_{film\ air}} * 100\ [\%] \qquad (9)$$

2.4.2. Combination of SPR and QCM-D data

The combination of both methods allows the determination the water content in the adsorbed layer.

$$\% water\ content = \frac{(mass_{QCM} - mass_{SPR})}{mass_{QCM}} \qquad (10)$$

3. Research objectives

Aim of the present thesis was the comprehensive surface study of a blend system with trimethylsilyl cellulose (TMSC) and hydroxypropyl stearate cellulose (HPCE) derivatives in different values of substitution degree and their interaction of the regenerated thin films to the blocking agent bovine serum albumin (BSA).

Based on different amounts of hydrophobic side chains in HPCE DS 1 and DS 3, varying microphase separation patterns are expected, which are further affected by various mixing ratios. In general, phase separated blend thin films have a higher roughness value compared to the neat films. The distinct polarities of the HPCE derivatives involve a fundamental different phase separation and might not fully separate laterally, based on the interaction on the solution-solid interface. [23] In HPCE DS 3 each hydroxy group is substituted with a bulky aliphatic C:18 chain, which are expected to have an extensive effect in dewetting of the polymer mixture while spin coating. This might result in a more coarsened phase pattern with bigger domains. The wettability depends on the surface free energy of the blend components, however is also affected by the morphology, like domain size and topography.

For protein interaction studies of the regenerated cellulose blend films BSA is chosen as a non-specific model substance. The pH value of blood is around 7.4, which is above the isoelectric point of BSA, where the protein has its least solubility and tends to agglomerate. Cellulose is known to be not very prone for non-specific protein adsorption, while BSA is expected to show enhanced adsorption to HPCE due the less solvation of the substituted stearate chains. Blend systems in literature did show interestingly no linear correlation of domain ratio in the surface with BSA adsorption and wettability. [11–13] The water content is expected to be lower for the HPCE films than for the neat cellulose films.

4. Experimental

4.1. Materials

Trimethylsilyl cellulose (TMSC) from Avicel was purchased from TITK (Thuringian Institute of Textile and Plastics Research, Rudolstadt, Germany) and used as received without any further purification. (M_w 185 000 g·mol^{-1}; M_n 30 400 g·mol^{-1}; PDI 6.1; DS 2.8). Hydroxypropylcellulose stearate (HPCE) was synthesized in the working group of Prof Biesalski (TU Darmstadt) according to a literature protocol and used as received with following specifications (M_w 134 700 g·mol^{-1}; M_n 107 400 g·mol^{-1}; PDI 1,25; DS 3.0; M_w 107 000 g·mol^{-1}; M_n 59 400 g·mol^{-1}; PDI 1,8; DS 1.0). [19]

Sulfuric acid - H_2SO_4 (95%), hydrogen peroxide - H_2O_2 (30%), chloroform – $CHCl_3$ (99.3%), hydrochloric acid – HCl (37%), diiodomethane (DIM) – CH_2I_2 (99%), sodium dihydrogen phosphate monohydrate ($NaH_2PO_4·H_2O$), disodium phosphate heptahydrate ($Na_2HPO_4·7H_2O$), and bovine serum albumin (BSA) (cold ethnol fraction, pH 5.2 ≥96%) were purchased from Sigma-Aldrich and were used as received. Monocrystalline silicon wafers from Siegert (Germany) were used as film substrates and were cut 1 cm × 2 cm. Gold sensor slides (CEN102AU) for surface plasmon resonance (SPR) measurements were purchased from Cenibra (Germany), containing a gold layer with 50 nm and a chromium adhesion layer of 5 nm. For QCM-D 5 MHz crystals with gold surface were purchased from QuartzPro (Sweden) and QSX 301 Gold sensors from QSensors (Sweden). Polymer solutions were filtered through CHROMAFIL® Xtra PVDF filters with 0.45 μm pore size purchased from Macherey-Nagel (Germany). Milli-Q water (resistivity = 18.2 MΩ·cm^{-1} at 25°C) from a Millipore water purification system (Millipore, U.S.A.) was used for contact angle, SPR, and QCM-D investigations.

4.2. Preparation and Cleaning of Silicon and Gold Substrate

For QCM-D and SPR determination Au-surfaces are used. For all other determinations monocrystalline Silicon wafers were used in a {110} direction cut and customized in a size of 1 cm x 2 cm by a diamond cutter. After rinsing the substrates, they were immersed into a Piranha solution, which was freshly produced by mixing 95% H_2SO_4 with 30% H_2O_2 in a 2 + 1 manner, for 30 min. The wafers were rinsed with deionized water properly, dried in a nitrogen steam and rinsed again to store them at least overnight in deionized water till the usage for spin coating.

Due to the higher fragility of the Au-layer, they were cleaned in a less invasive way, by using Piranha solution mixed in a 3 + 1 manner, which was cooled down to room temperature. New slides were immersed for 4 min, while reused slides with an applied film up to 8 min. Following, they were cleaned with MilliQ water, dried under N_2 stream, both steps twice repeated and stored in MilliQ water over night.

4.3. Preparation of Polymer Solutions

TMSC, HPCE in substitution degree (DS) of 1 and 3 were dissolved in chloroform in a concentration of 0.75 w%. All solutions were made in same manner, assisted by a magnetic stirrer for 120h using a water bath heated to 30°C. The solutions were filtered through 0.45 µm PVDF filters right before usage and mixed in volumetric ratios of 1+3, 1+1, 3+1 TMSC to HPCE, which are labelled further on as TMSC : HPCE 1:0, 1:3, 1:1; 3:1 and 0:1.

4.4. Preparation of thin films

For spin coating, the just filtered and mixed polymer solutions of 0.75 w% polymer in chloroform were used. A sample volume of 100 µl was spread on the substrate and operated for 60 s with an acceleration of 2500 rpm·s^{-1} up to 4000 rpm.

4.5. Regeneration of blend thin films

The selective conversion of the TMSC fraction in the thin films into cellulose was implemented in polystyrene petri-dishes with a diameter of 5 cm, by placing the substrate next to 3 ml of 10 w% HCl. The substrates were exposed to HCl vapor, by covering the petri-dish with its cap for 12 min. The completion of the reaction was verified by contact angle measurements and ATR-IR measurements. [83]

4.6. Removal of the HPCE fraction form the regenerated blend films

The HPCE phase is washed off selectively with chloroform. For the blends with HPCE DS 3 the substrate was tilted, and 0.5 ml chloroform were applied with a syringe drop by drop and let run down the surface. HPCE with DS 1 takes longer to get dissolved by chloroform, so the substrates were immersed to a beaker of chloroform for 70 s and washed afterwards as described above with another 0.5 ml chloroform.

4.7. Attenuated total reflectance infrared spectroscopy (ATR-IR)

ATR-IR spectroscopy was done with Alpha FT-IR spectrometer (Bruker; Billerica, MA, U.S.A.) using an attenuated total reflection (ATR) attachment. Spectra were obtained

in a scan range between 4000 to 400 cm^{-1} with 48 scans and a resolution of 4 cm^{-1}. The data was analyzed with OPUS 4.0 software.

4.8. Profilometer

By scratching the thin films with a scalpel, the thickness was determined, using a DETAK 150 Stylus Profiler from Veeco on a hydraulic balanced stone table. A profile over a scan length of 1000 μm and a duration of 3 s was measured with a diamond stylus with a radius of 12.5 μm, applying a force of 3 mg. The resolution was set to 0.333 μm and the measurement range was 6.5 μm. Three films of each sample were measured at 6 spots before and after regeneration. Film thickness and film roughness was calculated from the resulting profile by the related Software Vision 64.

4.9. Contact Angle (CA) and Surface Free Energy (SFE) Determination

Static contact angle measurements were performed with a Drop Shape Analysis System DSA100 (Krüss GmbH, Hamburg, Germany) with a T1E CCD video camera (25 fps) and the DSA1 v 1.90 software. All measurements were at least performed three times on minimum two manufactured films with Milli-Q water and diiodomethane using a droplet size of 3 μL and a dispense rate of 400 μL·min^{-1}. Using the the Young−Laplace equation static CA were calculated and the SFE was determined with the Owen-Wendt-Rabel-Kaelble (OWRK) method using surface energies for water (σ_{ls} = 72.8; $\sigma_{l,D}$ = 21.8; $\sigma_{l,P}$ = 51) and diiodomethane (σ_l = 50.8; $\sigma_{l,D}$ = 50.8; $\sigma_{l,P}$ = 0)

$$\sigma_{sg} \ = \ \sigma_{ls} \ + \ \sigma_{lg}\cos\theta \ \rightarrow \ \theta = \arccos\frac{\sigma_{sg} - \sigma_{ls}}{\sigma_{lg}} \qquad (11)$$

The interfacial tension σ_{sg} between solid and vapor σ_{sg}, is given by the sum of the interfacial tension between solid and liquid σ_{ls} and the x axis componence of the interfacial tension between liquid and vapor σ_{lg}.

By measuring the contact angle with different solvents, with known polar and dispersive fractions of the σ_{ls} interfacial tension, it is possible to calculate the surface free energy and its polar and dispersive fraction of the surface.

$$\sigma_{ls} \ = \ \sigma_{sg} \ + \ \sigma_{lg} - 2\left(\sqrt{\sigma_s^D * \sigma_l^D} + \sqrt{\sigma_s^P * \sigma_l^P}\right) \rightarrow \ \sigma_{ls} = \sigma_l^P + \sigma_l^D \qquad (12)$$

Since σ_{ls} is measured, plotting $\frac{1}{2} * (1 + \cos\theta) * \sigma_l / \left(\sqrt{\sigma_l^D}\right)$ over $\sqrt{\frac{\sigma_l^P}{\sigma_l^D}}$ and calculating the slope of the regression line gives the SFE of the surface. Finally, dispersive and polar fraction of the surface are calculated with Equation (12). [84]

4.10. Atomic Force Microscopy (AFM)

Surface morphology and roughness of the films were obtained in tapping mode in ambient atmosphere at room temperature. Measurements were done using a Veeco Multimode Quadrax MM scanning probe microscope (Bruker; Billerica, MA, U.S.A.) with Si-cantilevers (NCH-VS1-W from NanoWorld AG, Neuchatel, Switzerland) with a resonance frequency of 320 kHz and a force constant of 42 N·m⁻¹.

More sophisticated measurements were done by Caterina Czibula in Leoben in tapping mode under ambient conditions at 50 $\pm$ 8% relative humidity and a temperature of 22 $\pm$ 1°C. An Asylum Research MFP-3D AFM (USA) instrument was used, which is equipped with a closed-loop planar x-y-scanner with a scanning range of 85 µm $\times$ 85 µm and a z-range of 15 µm. A standard silicon probe by Olympus (AC160TS) with a spring constant of ~30N m⁻¹ and a radius tip of ~10 nm was chosen. For statistical analysis three independent positions were recorded for each sample. [85]

The data of all measurements were processed with the open-source software Gwyddion [86]: prerequisite, levelling the topography base line, aligning the rows by median of difference and calculating the root mean square (RMS) roughness σ.

Further, the 10x10 µm² AFM topography images were used for calculating surface fraction on the blend films. Therefore, the evaluated phase was masked by threshold in z-value. Adjustments were done with the pen tool and single noise pixels were removed by grain filtering function. The surface area was computed by simple triangulation, taking in response heights and spatial relations in the surface. For this purpose, extra points were added in-between four neighboring points using the mean values of these pixels. Like in Figure 15 shown, the connecting of the extra point to the neighboring pixels results in four triangles. Summing up these areas gives the surface area.
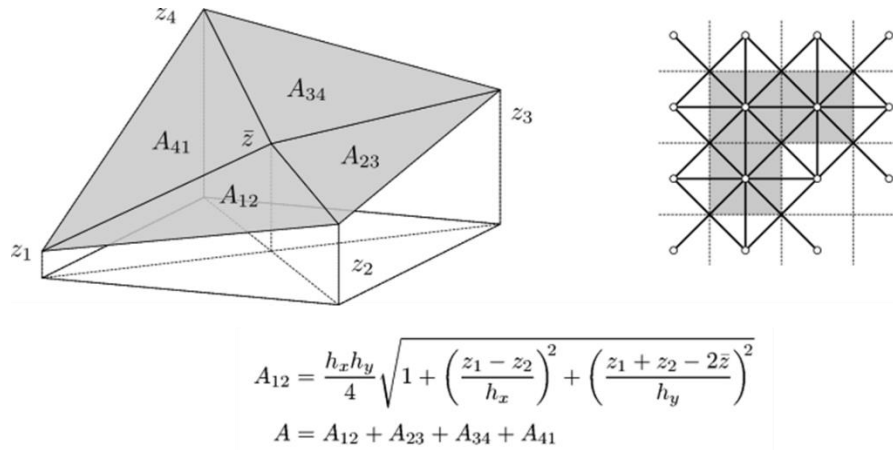
$$A_{12} = \frac{h_x h_y}{4} \sqrt{1 + \left(\frac{z_1 - z_2}{h_x}\right)^2 + \left(\frac{z_1 + z_2 - 2\bar{z}}{h_y}\right)^2}$$

$$A = A_{12} + A_{23} + A_{34} + A_{41}$$

Figure 15 Triangulation for computing the surface area in AFM topography [87]

4.11. Protein adsorption experiments

The adsorption experiments of bovine serum albumin (BSA) onto the present thin film surfaces were carried out in a phosphate buffer system (PBS) at pH 7.4. consisting of 8.1 mM disodium phosphate, 1.9 mM sodium phosphate and 100 mM NaCl. Therefore, 8.1 mmol disodium phosphate, 1.9 mmol sodium phosphate and 100 mmol NaCl were dissolved in 800 ml MilliQ water. The pH value was adjusted with 0.1 M NaOH and finally the volumetric flaks was filled to the one-liter mark. The adsorption was implemented with 1 mg·ml^{-1} BSA dissolved in the buffer for 10 min at 24.5°C.

4.11.1.   Surface Plasmon Resonance Spectroscopy (SPR)

The SPR measurements where quantified with a MP-SPR Navi 200 from Bionavis Ltd.: Tampere, Finland, using lasers at 670 and 785 nm in both measurement channels. The attached autosampler MP-SPR Navi 210A was set to 20 µl·min^{-1} flow rate. The equilibration manner of each thin film in buffer was observed by measuring the spectra with full angular scan (39-78°) and scan speed of 8°·s^{-1} and plot the SPR-angle over time to receive a sensogram. For data evaluation of the sensogram Δθ was determined as the difference of the value after 10 min washing time and the mean value of 5 min before the adsorption. Using the DeFeijter equation (4) the adsorbed mass was calculated. For the SPR Navi 200 k * dp was provided by bionavis as 1.09 x 10^{-7} cm/° (at 670 nm) and 1.9 x 10^{-7} cm/° (at 785 nm). The refractive index increment (dn/dc) for aqueous solutions of proteins reported in literature as 0.18 cm^3 g^{-1}. [88] For BSA it is reported as 0.187 cm^3 g^{-1}. [89,90]

4.11.2. Quartz Crystal Microbalance and Dissipation (QCM-D)

A quartz crystal microbalance and dissipation (QCM-D) instrument (model E4) from Q-Sense, Gothenburg, Sweden was used. The attached peristaltic pump was set to 0.1 ml min^{-1}. For each ratio four films were spin coated on QCM-D crystals and measured all at the same time. For estimation of the water content, the frequency shift for all gold crystals from H_2O to D_2O was determined before spin coating. All films were equilibrated in MilliQ water, until a stable base line was reached and afterwards rinsed with D_2O for 100 sec. For the BSA adsorption experiments MilliQ was replaced by PBS buffer with 8.1 mM disodium phosphate, 1.9 mM sodium phosphate and 100 mM NaCl at pH 7.4. 1 mg·ml^{-1} BSA in PBS buffer was adsorbed for 10 min and rinsed afterwards with buffer. Finally, the biopolymer film with adsorbed BSA was equilibrated to H_2O and exchanged D_2O for 100 sec, to determine the water content of the film with adsorbed BSA.

5. Results and Discussion

5.1. Preparation of blend thin films

During laboratory work, the dissolution of the biopolymer turned out to be one of the crucial steps for developing macroscopically smooth and homogeneous thin films. Especially HPCE tended to agglomerate in solution, which hints to rough thin films with particles included at the surface. These were depicted by AFM as protrusions with diameters in the range of about one micrometer. Their elevation was about 400 nm – 1000 nm. (see Figure 16) To overcome this drawback, a long-term preparation of well solvated macromolecules combined with a final filtering step was employed. The solutions mentioned above were stirred for 120 h using a magnetic stirrer at 40 °C with a temperate water bath until a homogenous solution was obtained. All solutions were treated the same way. To avoid aggregation of the macromolecules and to prepare homogenous solutions an ultrasonic bath was used for 10 min and a filtering step was implemented immediately afterwards. Although the TMSC required far less time (about 3 h) to dissolve, all polymers were treated the same way as the HPCE DS 1 derivative. Additionally, it has been figured out that less particle agglomeration was observed, when there was no time delay between filtering, mixing the solutions in the defined ratios and the final spin coating.
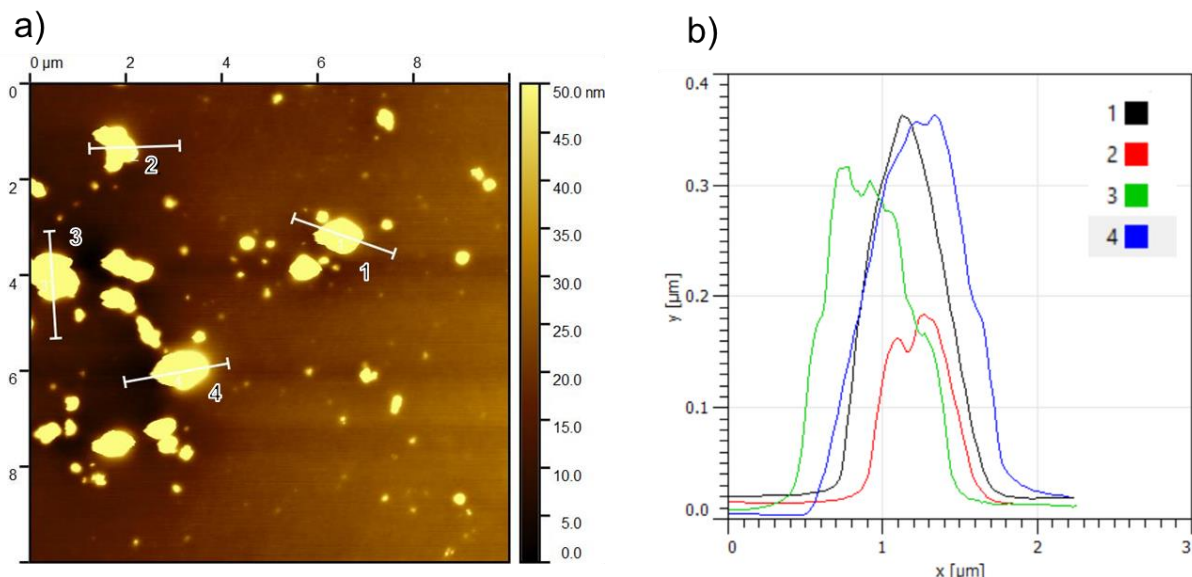
Figure 16 Dimensions of elevation and diameter of protrusions in a pure HPCE DS 1 film – unfiltered.(a) 10 x 10 µm² AFM topography image. (b) Cross sections along the lines masked in (a).

5.2. Regeneration observation by ATR-IR

For monitoring the regeneration conversion, ATR-IR spectra of each film were recorded. 12 min exposure time was found to be enough to fully remove all trimethylsilyl groups, which is in accordance with values reported in literature. The according spectra are shown in Figure 17. The Si-CH$_3$ deformation and Si-O-C stretching vibrations bands in 1252, 885, 848, and 756 cm^{-1} decrease, while the a broad band 3700 - 3000 cm^{-1} appears due to OH-stretching band. [91]
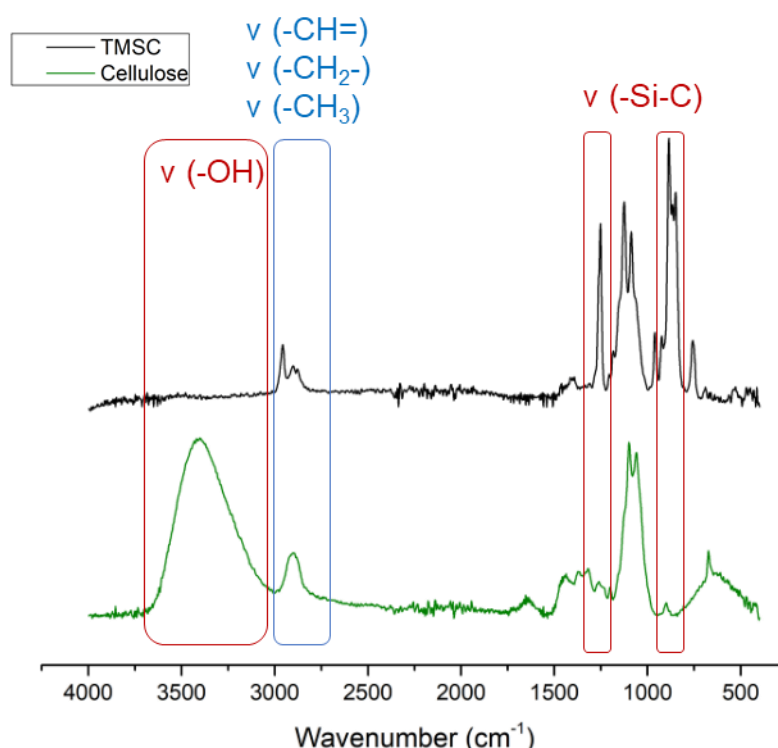
Figure 17 ATR-IR spectra of TMSC and regenerated cellulose after 12 min regeneration time with 10 w% HCl.

While TMSC undergoes a chemical reaction through exposure to HCl vapor, the hydroxypropyl stearate cellulose is stable as shown in Figure 18. As expected, the intensity of the carbonyl stretching vibration at 1734 cm^{-1} decreases in intensity with the degree of substitution, the same holds for the CH-stretching bands of CH$_3$ and CH$_2$ at 2921 and 2852 cm^{-1} as well. Due to less substitution of the HPCE DS 1 with

hydroxypropyl stearate there are more unsubstituted OH groups left and the OH-stretching vibration (~3100 -3600 cm⁻¹) is increased.
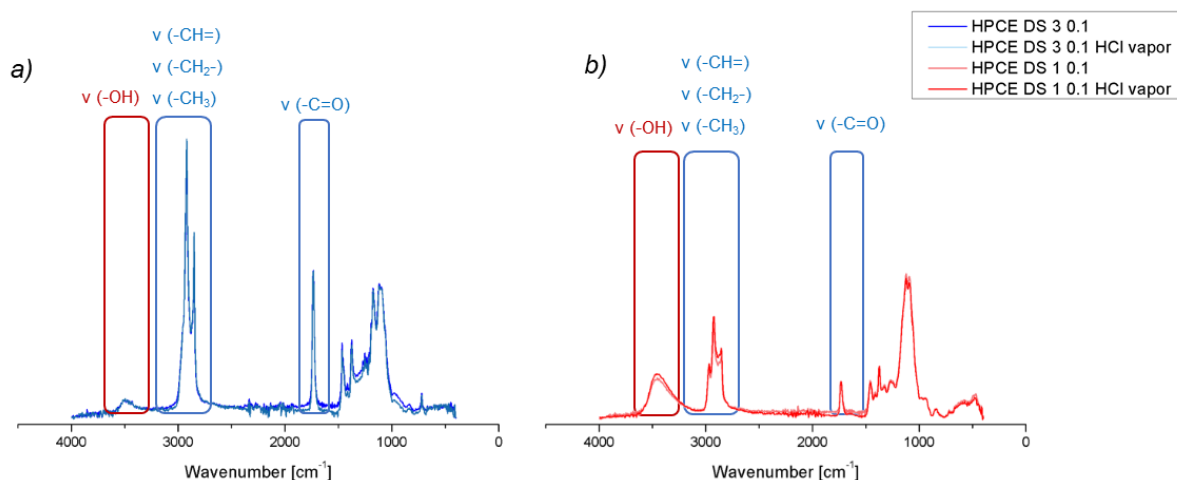
Figure 18 ATR-IR spectra of HPCE films before and after regeneration procedure. HPCE DS 3 (a) and HPCE DS 1 (b) undergoes no conversion.

All relevant bands are summarized in Table 3.

Table 3 Adsorption bands of ATR-IR spectra of TMSC, regenerated cellulose and HPCE films [16]

IR-frequency [cm⁻¹]		Absorption bands
3700 – 3000	broad band	OH-stretching band
2800 – 3000 2921, 2852	v sym. stretch (C-H)	CH-stretching bands of CH₃, CH₂
1252, 885, 848, and 756		Si-CH₃ deformation and Si-O-C stretching vibrations
1000 – 1200		C-O stretching vibrations of cellulose backbone and
1735	v stretch (C=O)	C=O stretching bands of

For the blend thin films after regeneration the Si-CH₃ deformation and Si-O-C stretching vibrations disappear [1] and a broad OH-stretching band in arise. The peaks due CH-stretching vibrations remain unchanged, like depicted in Figure 19.
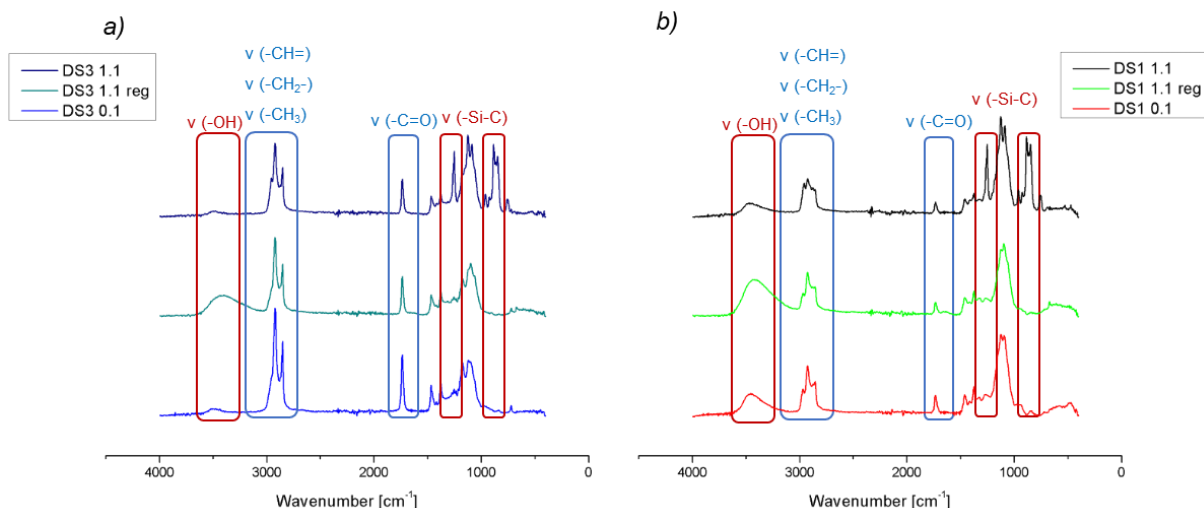
Figure 19 ATR-IR spectra of blend films in 1:1 ratio with HPCE DS 3 (in the left) and DS 1 (in the right) before (spectra in first row) and after regeneration (spectra in the middle) in context with the neat HPCE film (lowest spectra)

5.3. Film thickness

After spin coating, the TMSC bend thin films have a film thickness of 85 nm to 130 nm. As mentioned in the introduction, regeneration of TMSC thin films to cellulose leads to shrinkage of the films by removing the trimethylsilyl group with HCl vapor. Here, this results in a film contraction of 60 % ± 3.6 % in film height for the pure cellulose films, which is in good agreement with the literature. [10,83] As expected, the HPCE films do not shrink, since they do not get regenerated by the HCl vapor. (see Figure 20)
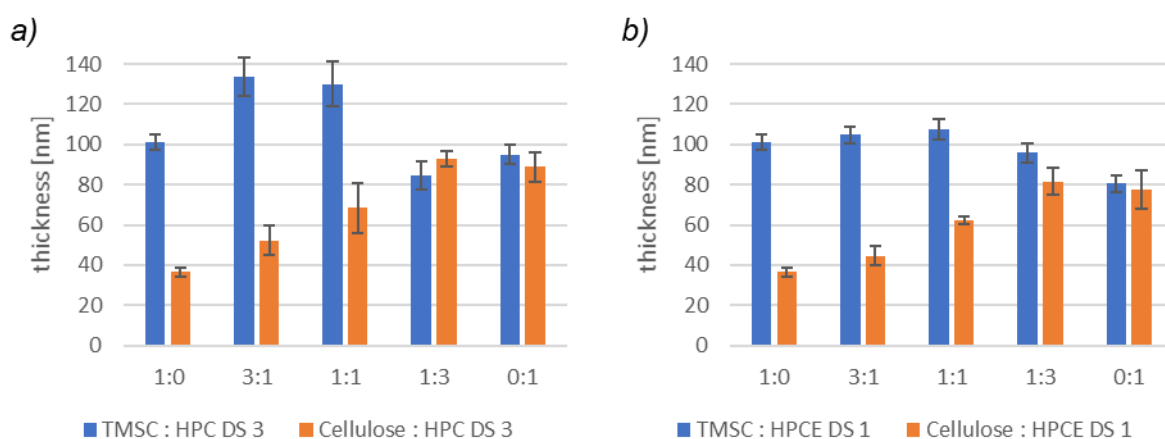
Figure 20 Film thickness of TMSC : HPCE blend films in blue and regenerated Cellulose : HPCE in orange (a) HPCE DS 3 and (b) HPCE DS 1 determined by profilometer

Interestingly enough, some of the blend films turned out to be thicker than the pure films. Especial apparent is this observation for the blend films of TMSC : HPCE (DS 3)

37

in ratios 3:1 and 1:1. However, this tendency is not present in the film of 1:3 ratio, which thickness is in the same range as the pure films. Also, the blend films with DS 1 do not get significantly thicker. The effect of increasing film thickness of the blends is known from micro phase separated thin films from literature. For TMSC/PHB blends the largest increase of thickness is shown in the 3:1 ratio (+60% in relation to TMSC films from chloroform ~100nm). While a high PHB content does not effects the thickness increase that much, a high TMSC content – rapid beginning from 3:1 ratio – results in thicker films. [12] In TMSC/CSE blends there is almost no increase in film thickness recognizable.

Like described later in Chapter 5.5, in ratio 3:1 and 1:1, large TMSC domains are protruding on the HPCE DS 3 matrix, due to the phase separation. These islands in 3:1 ratio are ~ 1 µm in diameter and about 80 nm lower than the TMSC matrix. Since the profilometer probe has a radius of 12.5 µm, the lowered HPCE phase is not detectable and the measured film thickness is caused by the TMSC island. The same effect is expected in the 1:1 ratio, where TMSC enriched phase was detected by AFM phase image, as random pattern in the µm range. In the 1:3 ratio the domains are much smaller (droplets ~ 200 nm in diameter, protruding ~ 45 nm). The smaller volume is presumed to be the reason for less protruding of the TMSC phase. In the TMSC : HPCE DS 1 blends the domains are in the range of 200 – 1000 nm and there was no increase of the thickness for the blends detected by profilometer as well. From the present measurements the effect of thicker blend films than pure films is expected to be a function of domain size.

5.4. Surface free energy

The conversion of TMSC to cellulose results in decreasing static contact angles due to the removal of the trimethylsilyl groups and the formation of hydroxy groups instead. Pure TMSC was evaluated to have a static contact angle of 94° ± 1° with water and 65° ± 1° with diiodomethane (DIM) by using the Young-Laplace equation. After regeneration the contact angled decreased to 36° ± 1° wettability for H_2O and to 33° ± 1° for DIM.
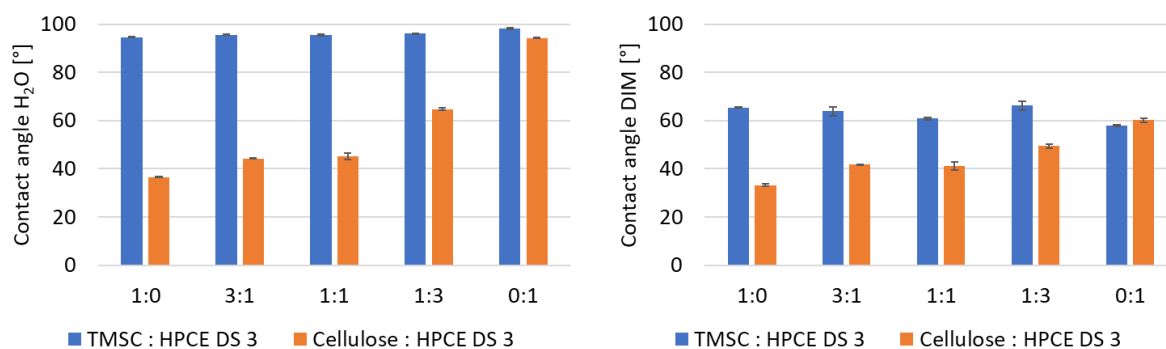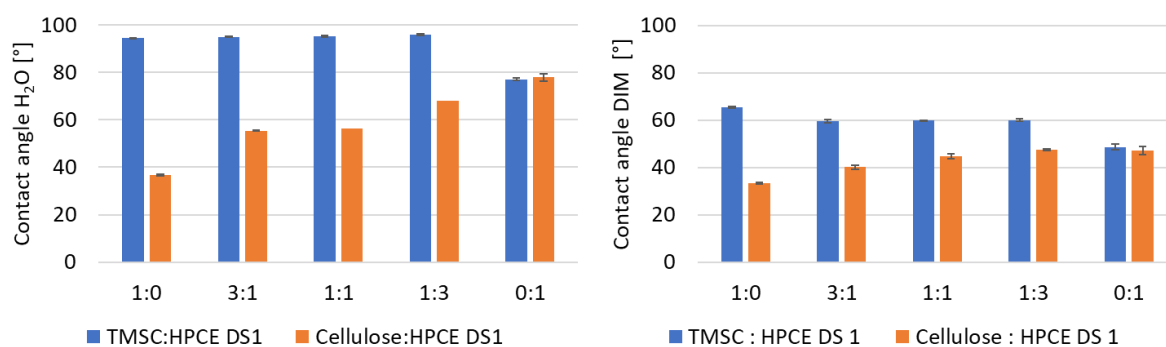
Figure 21 Static contract angle for TMSC : HPCE DS 3 blends (blue) and the regenerated film (orange) for H$_2$O (a) and DIM (b) as wetting solvents.

While the wettability is highly affected by regeneration for TMSC films, the values for pure HPCE films do not change significantly with exposure to HCl. Small deviations are due to measurement of various manufactured thin films. On pure HPCE DS 3 films, water CA of 98° ± 1° and DIM CA of 58° ± 1° were determined. (See Figure 21) Based on the chemical structure of the less substituted HPCE DS 1, the wettability should increase. Indeed, the surface of pure HPCE DS 1 films were quantified with a water CA of 77° ± 1° and a DIM CA of 48°° ± 2°. (See Figure 22) For the regenerated blend thin films, a trend of decreasing CA according to the raising cellulose ratio was observed.

Figure 22 Static contract angle for TMSC : HPCE DS 1 blends (blue) and the regenerated film (orange) for H$_2$O (a) and DIM (b) as wetting solvents.

With the Owen-Wendt-Rabel-Kaelble (OWRK) method [84], the surface free energy was calculated. For TMSC, a SFE of 27 ± 1 mJ·m^{-2}, with 25 ± 1 mJ·m^{-2} disperse and 2 ± 1 mJ·m^{-2} polar part was determined. (see Figure 23 and Figure 24) For regenerated cellulose, the SFE considerably increases to 67 ± 1 mJ·m^{-2} with a disperse ratio of 43 ± 1 mJ·m^{-2} and a polar ratio of 24 ± 1 mJ·m^{-2}. These values are in good correlation with literature. [13]
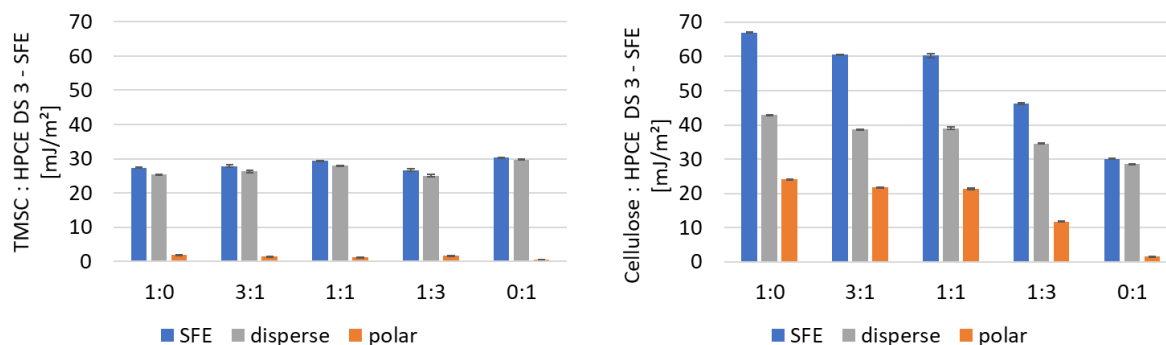
39

Figure 23 Surface free energy of the TMSC : HPCE DS 3 blend films (a) and regenerated films (b) calculated by Owen-Wendt-Rabel-Kaelble (OWRK) method with disperse and polar ratio.

The SFE for pure HPCE DS 3 was estimated with 30 ± 1 mJ·m^{-2} total and a polar ratio of 2 ± 1 mJ·m^{-2}. The SFE of HPCE DS 1 with 41 ± 1 mJ·m^{-2} has a bigger polar ratio of 6 ± 1 mJ·m^{-2}. Therefore, difference in SFE is larger between TMSC and HPCE DS 1 than for the TMSC : HPCE DS 3 blend system and results in a fundamental by different phase separation behavior and finally ends up in different micro pattern. (see Chapter 5.6 Phase separation behavior in thin films)
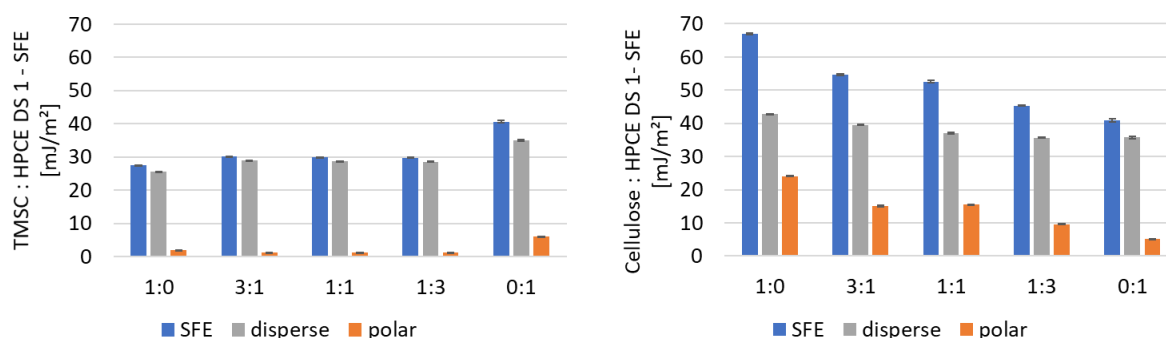

Figure 24 Surface free energy of the TMSC : HPCE DS 1 blend films (a) and regenerated films (b) calculated by Owen-Wendt-Rabel-Kaelble (OWRK) with disperse and polar ratio.

40

5.5. Surface Topography by AFM

As found in literature, thin films from polymer mixtures show microphase separation on the micrometer scale. [23,92] Figure 25 illustrates schematically the expected sequence of surface morphology alterations due to regeneration and washing steps in blend thin films, starting from a phase separated thin film (Figure 25 a). By regeneration, the bulky trimethylsilyl group is split off as verified by ATR-IR due to regeneration (see chapter 4.7). This results in contraction in volume of the cellulose domains, which leads to inversed height patterns of the regenerated films (Figure 25 b). By washing off HPCE domains with the former used solvent $CHCl_3$, the pattern can be inversed again (Figure 25 c). Since the AFM method reveals true height information, the separated domains in the present blend films can be detected by tapping mode AFM.
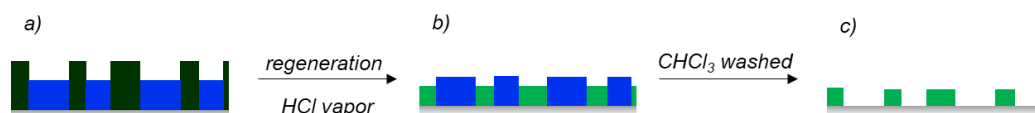

Figure 25 Influence of the regeneration on film thickness - schematic representation. TMSC enriched phase (dark green) blended with HPCE (blue) (a). Exposure to HCl vapor regenerates TMSC to cellulose (green), which results in contraction of the phase (b). Washing the regenerated blend film with chloroform the cellulose patterns remains. (c)

5.5.1. TMSC - HPCE DS 3 blend system

Topography and roughness parameters

Figure 26 a) shows 10 x 10 µm^2 topography images of TMSC:HPCE DS 3 blends and the related pure films. Depending on the mixing ratio, different phase-separated patterns do form. While in 3:1 blends HPCE DS 3 is spinodal decomposed close to bicontinuous phase and builds big islands in TMSC matrix, in 1:1 and 1:3 blends TMSC forms protrusions in HPCE matrix. After regeneration the resulting cellulose phase is contracted and at a lower height level than the HPCE phase. (see Figure 26 b)
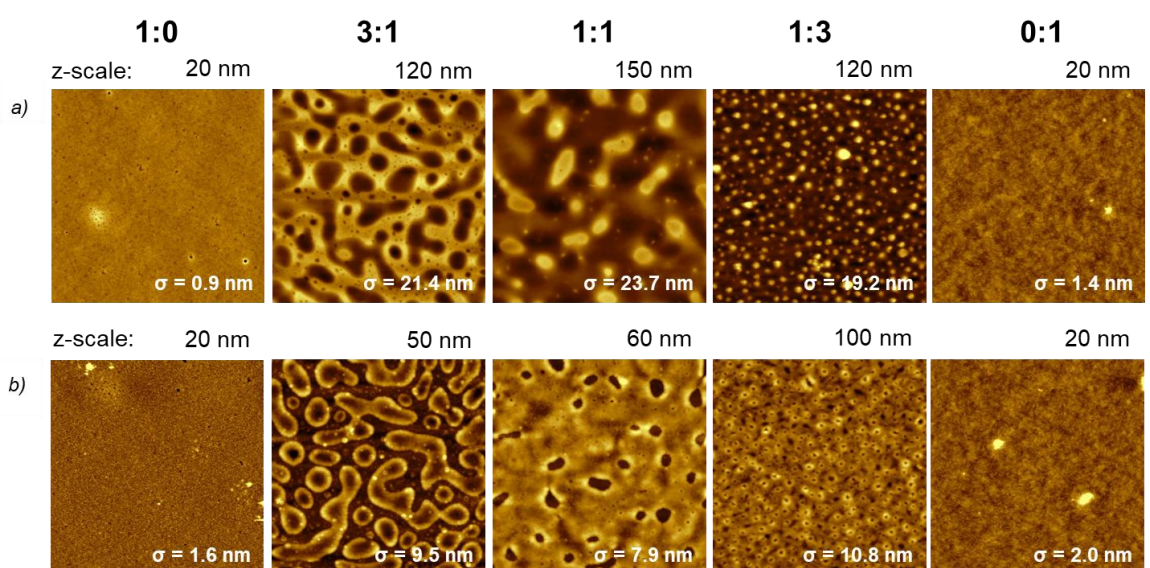

*Figure 26 10 * 10 µm^2 AFM topography images in tapping mode a) TMSC : HPCE DS 3 not regenerated thin films; b) Cellulose : HPCE DS 3 regenerated thin films, the corresponding z-scales and resulting σ values are given in each image.*

Integral information on the height difference between the polymer phases are reflected in the σ value of the height images. It expresses the root mean square (RMS) deviation of the height irregularities computed from the data variance of each image pixel and represents a measure for the vertical surface roughness. The corresponding values are presented in each image of Figure 26 and plotted in Figure 27 as a function of mixture ratio.

As expected, the neat films have a smooth surface with σ values in the range of a few nm. Phase separation results in a significant increase in σ values, by a factor of about 10 for the TMSC based blend films and by a factor of 5 for the regenerated cellulose blend films. corresponding standard deviations are plotted in Figure 27.
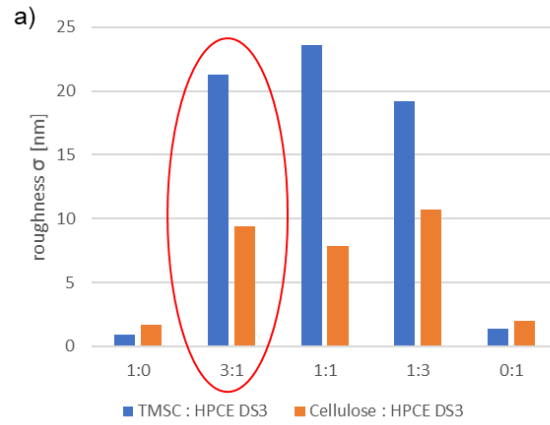
Figure 27 σ-values of the preliminary AFM topography and b) of the comprehensive surface roughness analysis of three independent 5 x 5 µm² topography images taken from Czibula et al 2019 [85] of the HPCE DS 3 blends before and after regeneration.

Calculation of the surface ratio of each phase

If the height difference between the separated phases is high enough, height distributions in height histogram can be used to calculate the surface ratio of each phase. However, the peaks of height distribution are not well resolved for all HPCE DS 3 blend films. For this reason, the evaluated phase was masked in Gwyddion by a threshold in z-value in each topography. In Figure 28 the masked AFM topography images are depicted.
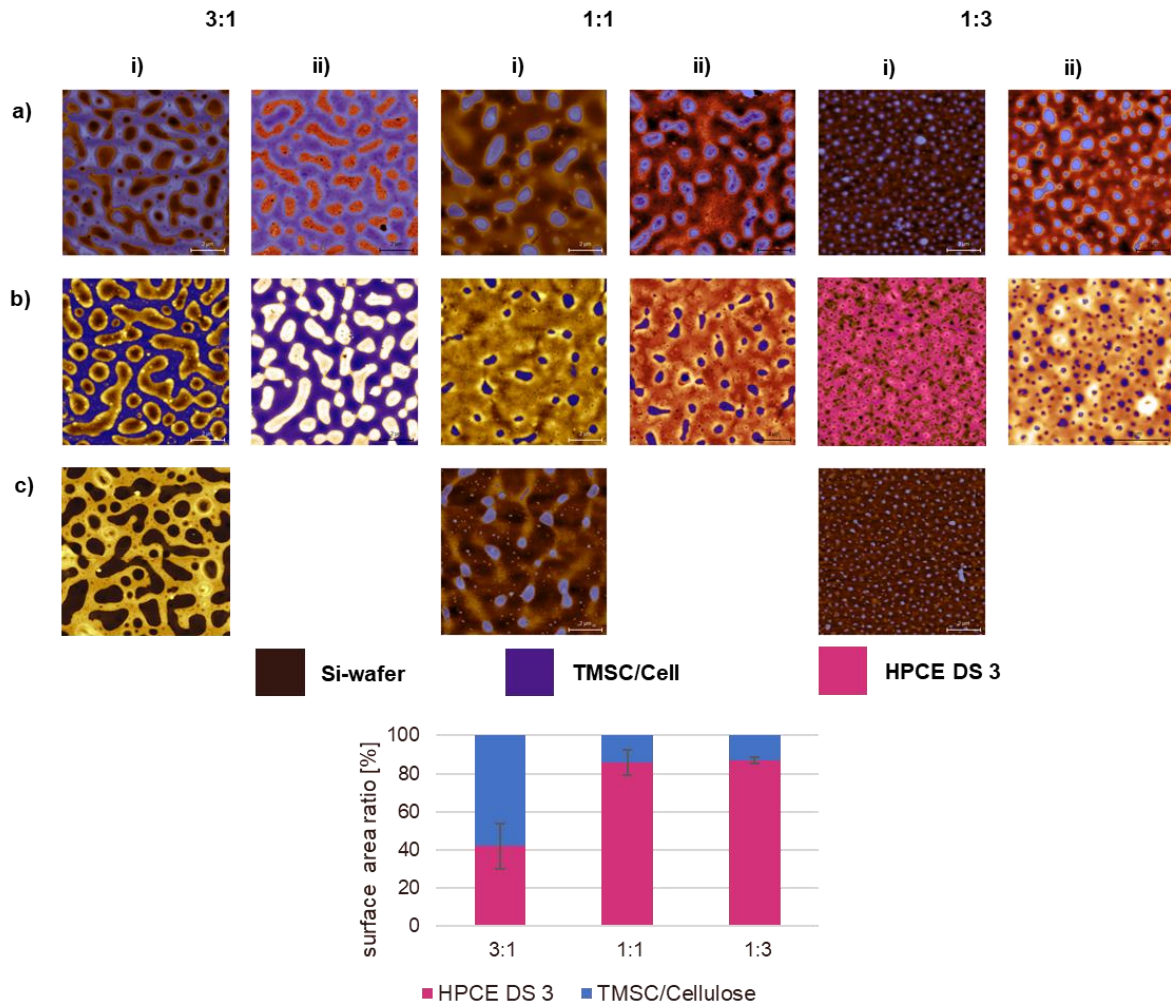

Figure 28 Masks for the surface area estimation of 10 x 10 µm^2 AFM topography of preliminary (i) and the final (ii) measurements with the exception of 1:3 ii) measurements: 5 x 5 µm^2 a) TMSC : HPCE DS3; b) regenerated Cellulose : HPCE DS 3 c) chloroform washed Cellulose structure – same z-scales as in Figure 26

The resulting surface area fractions were unexpected especially in terms of the 1:3 and the 1:1 ratio, where the cellulose proportion seemed to be underestimated. Taking a closer look at the height images of the chloroform in the 1:1 ratio, additional areas (~20 nm in diameter) appear, besides the marked phase separated islands of ~100 nm diameter (see in Figure 30). Therefore, this additional cellulose was sought for in the

44

cellulose : HPCE DS 3 films. Aligning the phase image to the topography, an effective surface fraction of 38% could be determined.

AFM images of the 1:3 ratio with larger magnification show a very interesting mixed phase. Needle-like dendrite structures grow from the regenerated cellulose phase into the enhanced HPCE phase, which is darker shaded in the phase image. (see Figure 29). Considering these the surface fraction of the TMSC respectively the regenerated cellulose is determined as 74 % and 58 % for the regenerated film.
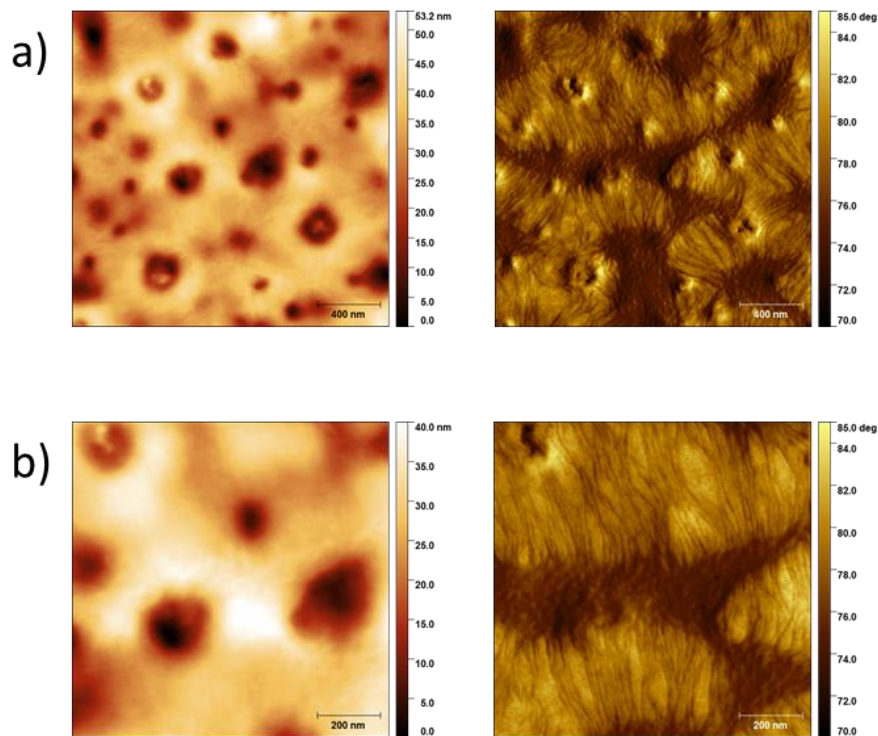

Figure 29 From [85]: Topography and according phase images of regenerated Cellulose : HPCE DS 3 in 1:3 ratio, (a) 2 x 2 µm² und (b) 1 x 1 µm². The TMSC phase extends as fine strings into the HPCE matrix.

The surface fractions for the TMSC : HPCE DS 3 (blue diamonds) films and the relating regenerated films (grey circles) were estimated and consulted for the further considerations as effective surface fraction. In the diagram of Figure 30 d) it is obvious that the surface fraction does not fit the volume fraction, as it was mixed in the applied solution.
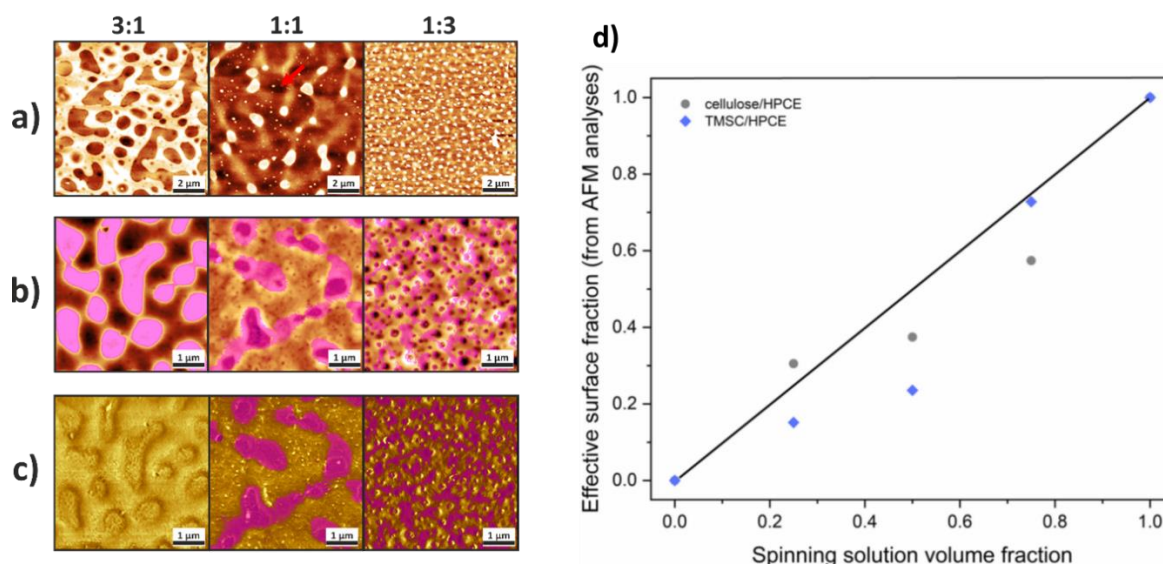
Figure 30 From [85]: Estimation of effective surface fraction from the 10 x 10 μm² preliminary topography of the chloroform washed films (a), the 5 x 5 μm² final topography of the regenerated Cellulose: HPCE DS 3 films, (b) and the related 5 x 5 μm² phase images (c). Effective surface fraction from AFM analysis as a function of the spinning solution volume fraction (d).

Phase separation behavior according to the transient bilayer theory

Proven by AFM topography measurements of the chloroform washed regenerated films, in all three ratios the TMSC enriched phase was found to be the enhanced phase towards the HPCE phase. The maximal substitution degree of cellulose with propyl stearate ester in HPCE DS 3 implies a high concentration of fatty acid chains. Therefore, the material has low surface energy and is expected to be located at the polymer-air interface in the initial bilayer status, while TMSC should be enriched at the oxidized Si surface. As the solvent evaporation proceeds, the upper phase starts to dewet, based on interfacial instabilities, due to the nascent concentration gradient. From the dissolving procedure it was experienced that TMSC was dissolved in chloroform fastest. Therefore, it can be presumed that TMSC is better soluble in chloroform, without any further quantification. Hence, the TMSC enriched phase is expected to stay swollen in solvent for longer time during spin coating. In literature it is described, that as a result of reduced mobility of the partially dried thin films, the better soluble phase finally collapses. [38] In contrast, in the present blends the influence of low surface free energy seems to be dominant that much, that even after complete solvent evaporation the TMSC is enhanced.

In the 1:3 ratio, a thick top layer of HPCE dewets and starts to break up, during spin coating. The generated holes are subsequently filled by the TMSC from below. The phase images show a mixed phase, were strings of TMSC reach into the HPCE matrix.

(see Figure 29) Such a morphology is far from thermodynamic equilibrium. It is expected, when annealing a spin coated 1:3 blend thin film above the T_g of the phase with the lower T_g, that in the equilibrium state a morphology with TMSC droplets in HPCE DS 3 matrix is preserved. [37,38]

The phase images of the 1:1 ratio revealed that TMSC is not just found in the enhanced domains. (See Figure 30) in the chloroform washed cellulose : HPCE DS 3 blends single small agglomerates (~20 nm) were found as well as an additional thin layer cellulose beside the domains. The bulky propyl stearate residues on the HPCE might stabilize the bilayer state and hinder a full vertical stratification of the TMSC phase. [36]

In 3:1 ratio, big islands HPCE DS 3, which consist of multiple coalesced droplets (1-2 µm in diameter) are embedded in an enhanced TMSC matrix. This phase structure is close to spinodal phase separation, which is expected in a blend system were polymers are mixed in same molecular ratio.

Correlation of SFE values with AFM roughness parameters and surface fraction analysis

From the AFM topography analysis the surface fractions for TMSC : HPCE DS 3 blend system are calculated and put into context with the surface free energy. It is known, that roughness of surfaces affects the wettability and therefore the Young contact angle (see Figure 31). [93]

The cellulose : HPCE DS 3 1:1 ratio has an unexpected high surface free energy. The regenerated 1:1 ratio shows the smoothest film surface of the examined blends (σ = 8 nm). The better wettability of even surfaces might be an explanation for the plateau in SFE at the 1:1 ratio.
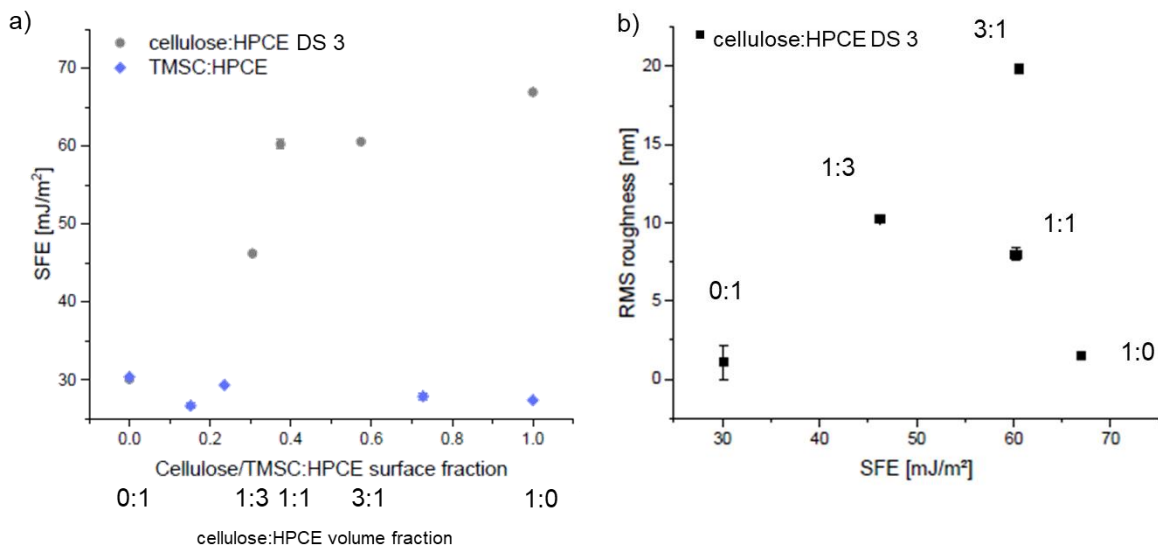

Figure 31 From [85]: SFE of TMSC HPCE DS 3 (blue diamonds) and regenerated Cellulose : HPCE DS 3 (grey circles) as function of SFE (a) and RMS roughness contrasted to the SFE.

5.5.2. TMSC - HPCE DS 1 blend system
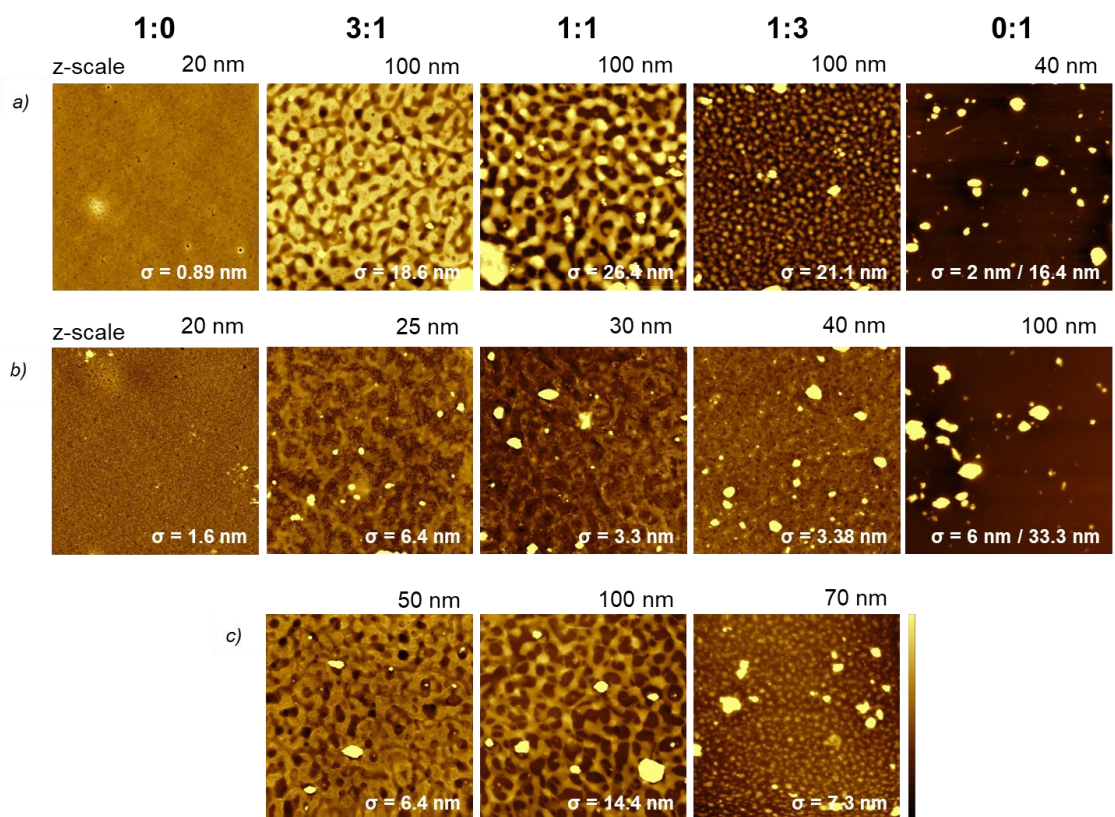
Topography and roughness parameters

Figure 32 10 x 10 µm² AFM mapping in tapping mode a) TMSC : HPCE DS 1 not regenerated thin films; b) Cellulose : HPCE DS 1 regenerated thin films, all solutions were not filtered c) patterned Cellulose after CHCl₃ washing; the corresponding z-scales and resulting σ values are given in each image.

In contrast to the blends with HPCE DS 3, the morphology of the blends with DS 1, presented in Figure 32, results in much smaller domains. The measurements of unfiltered films show many agglomerated particles, which are 200 to 1000 nm in diameter and up to ~40 nm protruding from the film surface.

The roughness evaluation via the RMS value yields integral information on the height difference and is therefore affected by the agglomerated particles. By the masking function of the Gwyddion software these particles were excluded from the σ value estimation. Especially for the pure HPCE DS 1 films, a lot of irregularities were monitored and σ-values > 30 nm were obtained. Considering only the smooth parts of the pure films, the expected low values were found in the range of 1 – 10 nm. Contrary to the pure films, the microphase separation of the blends with TMSC and HPCE (DS 1) results in σ-values about 20 nm. After regeneration the TMSC contracts and in this blend system both phases level almost at the same height (see Figure 34). The corresponding values are presented in each image of Figure 32 and plotted in Figure

33 as a function of the mixture ratio. Since only one spot on each film was contemplated by AFM, no extensive statistics with standard deviations were accessible.
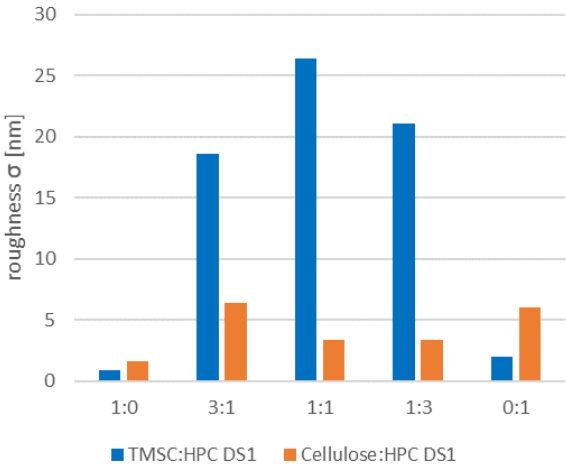

Figure 33 σ-values of the AFM topography of unfiltered HPCE DS 1 blends before and after regeneration.

The TMSC phase is about 50 nm evaluated on the HPCE DS 1 phase. During regeneration, the TMSC contracts and the phase level shrinks down almost to the same height as the HPCE phase. Hence, it is not possible to distinguish the phases from the topography with a resolution of 10 x 10 μm^2. To visualize the surprisingly even morphology of the regenerated Cellulose : HPCE DS 1 in 1:1 ratio, representative profile lines of a TMSC : HPCE DS 1 film, a regenerated film and a film, which was chloroform washed after regeneration, were plotted in a diagram in Figure 34.
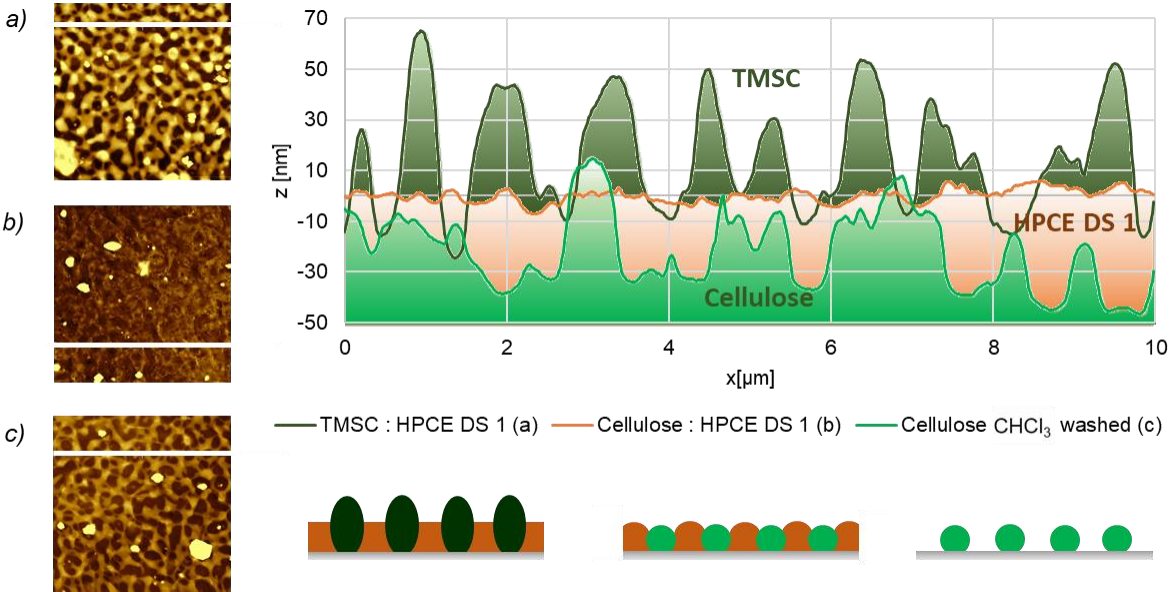

Figure 34 Profile lines of TMSC : HPCE DS 1 in 1:1 ratio (a), a regenerated film (b) and a chloroform washed film (c), for visualization of the topography modification by regeneration and rinsing of the HPCE phase.

Phase separation behavior according to the transient bilayer theory

In all three blend ratios, TMSC turns out to be the protruding phase, which was proven by AFM measurements of the according regenerated and further chloroform washed thin films. Based on the surface free energy (SFE) of each polymer, the solution of one polymer either enriches on the air interface or on the substrate interface and is the basis for the resulting microphase separation pattern. The SFE was determined by the Owens-Wendt method from contact angle measurements and determined as 41 mJ·m^{-2} with a polar ratio of 5.5 mJ·m^{-2}. In contrast, TMSC thin films were found as less polar with an SFE value of 27 mJ·m^{-2}, with 25 mJ·m^{-2} disperse and 2 mJ·m^{-2} polar ratio (see Chapter 5.4). Therefore, HPCE DS 1 is expected to form the bottom layer on the surface polymer interface and TMSC the top layer on the polymer air interface according to the transient bilayer theory.

As the solvent evaporation proceeds, TMSC starts to dewet, breaks up, and voids get filled from the HPCE DS 1 beneath. In the 1:1 ratio, microphase separation results in a bicontinuous spinodal demixing pattern. Meanwhile, in the 1:3 ratio a thin TMSC layer, dewets and constricts into circular droplets, which are ~ 200 nm in diameter and protrude ~30 nm on the HPCE DS 1 matrix. In the 3:1 ratio, a thicker TMSC layer dewets and small voids are filled with HPCE DS 1 from beneath. This results in ø ~ 200 nm cavities of HPCE enriched phase, which are about 50 nm lower than the surface of the TMSC matrix.

5.6. Phase separation behavior in thin films

5.6.1. TMSC – HPCE Blend systems in terms of different DS

In the following chapter, the blend systems of TMSC and HPCE with DS 3 and 1 are compared in terms of the transient bilayer theory, which was developed by Walheim, Böltau et al. 1997 [23] and verified by Heriot, Jones, 2005 [31]. Therefor representable profile lines of each blend film are depicted in Figure 35.
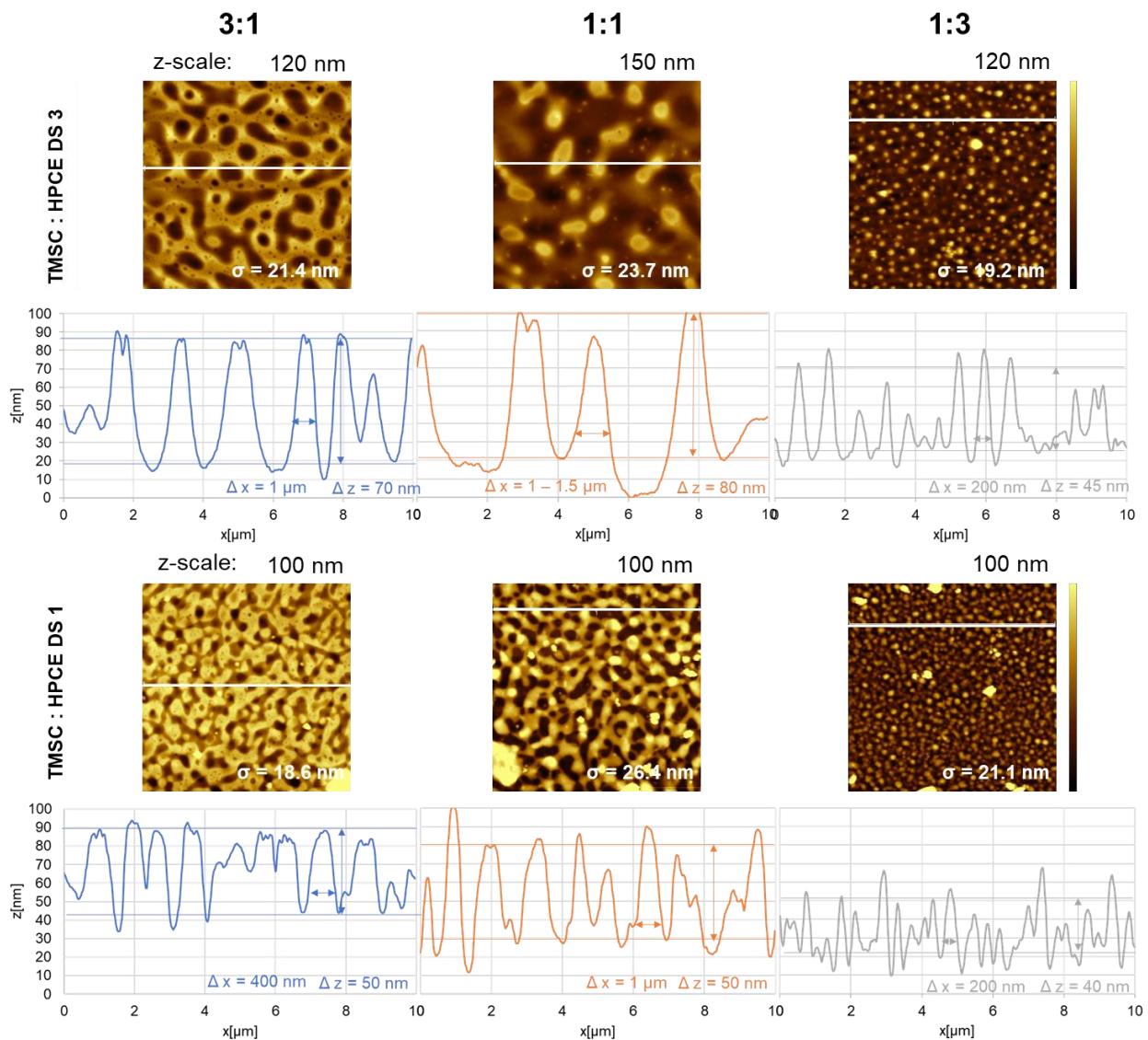
Figure 35 10 x 10 m² AFM topography of TMSC/HPCE blend systems with different degree of substitution. In the upper row DS 3 and in the lower row DS 1. The enhanced domains were proved to be the TMSC enriched domains (see chapter 6.2)

In all cases TMSC forms enhanced domains, which was proven by AFM analysis of the regenerated and chloroform washed films. (see Figure 26 and Figure 32). Based on the chemical structure, TMSC is expected to form the bottom layer in the blend system with HPCE DS 3, and the other way around in the case of HPCE DS 1.

Comparing the blends of TMSC/HPCE in different degree of substitution, it is obvious that the microphase separation patterns of DS 3 are coarser than in DS 1. In both cases, the mixture of 1:3 ratio results in protruding droplets of TMSC, which are homogeneous distributed. In the phase image of the blend with HOCE DS 3, needle like intentions into the HPCE phase are detectable. Since HPCE DS 1 is very similar to cellulose, phase images were net detectable with the derivative DS 1. While the 1:1 ratio with HPCE DS 1 forms a quite fine spinodal demixing pattern, were also the HPCE phase is almost continuous, in the blend with HPCE DS 3 TMSC is not only located in the protruding islands of ~ 1000 nm diameter, but also in the enriched parts of the lower matrix, what is displayed in the phase images. (see Figure 30 c). Spinodal decomposition is expected in mixtures with same molecular ratio. In the blends with HPCE DS 3 this was the case close to the 3:1 ratio. Never the less, this structure is much coarser.

In HPCE DS 3, all available hydroxy groups of the HPC are esterified with bulky non polar stearic acid, while in DS 1 just one third of the fatty acid is present, consequently HPCE DS 3 has a higher molecular weight. It has been proven by neutron reflectivity that polymers with higher molecular weight show broader interfacial width in initial bilayer state. This might be caused by reduced mobility of the bigger molecules. [30] The high amount of bulky fatty acid chains might further stabilize the interfacial width, which may explain the coarser structure in DS 3 blend series.

In the profile lines of TMSC : HPCE DS 3 1:1 and 3:1, it is remarkable that there are protrusion, which seem to have indentations of 5 – 10 nm. It is known, that the applied force under the AFM tip can be locally high, based on the spring constant of the cantilever and amplitude and frequency of the tapping mode. The contact pressure may result in indentations [94,95]. In both series, stiff (spring constant k = 30 mN. m^{-1}; 42 mN·m^{-1}) cantilevers were used, so the measurements should be comparable. In tapping mode, the amplitude is taken as a constant set point. High amplitudes may compress polymers beneath.

5.7. Surface interactions with proteins (BSA)

Surface interactions were determined for HPCE DS 3 only. Preliminary determinations for regenerated cellulose : HPCE DS 1 blends are shown in the outlook.

5.7.1. SPR measurements

As expected, the films with higher HPCE DS 3 content tend to need longer to reach the equilibrium state film in buffer. The mean equilibration time for pure cellulose films was about 77 ± 45 min and for pure HPCE DS 3 films 167 ± 63 min.
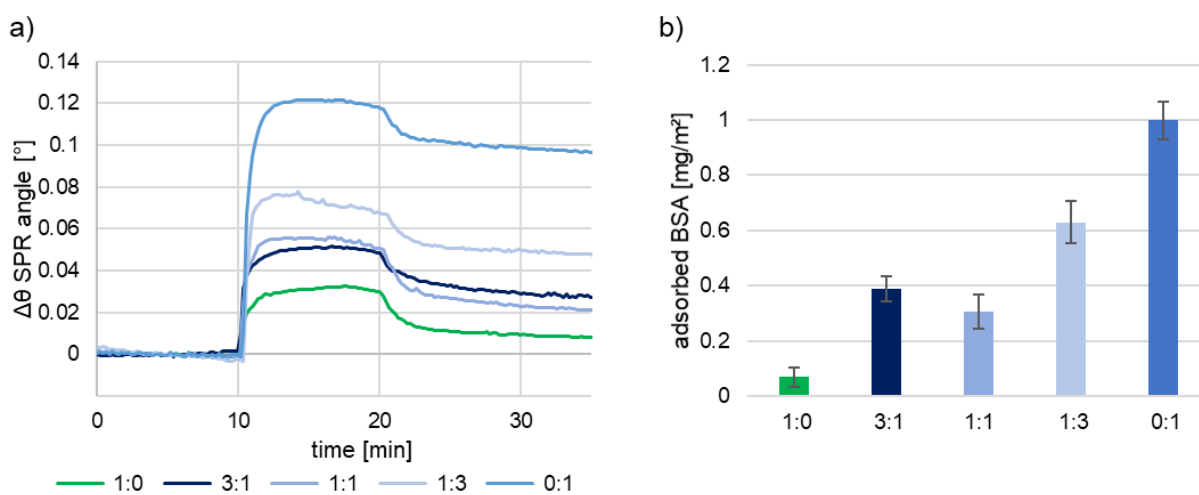

Figure 36 SPR measurements of 1 mg·ml⁻¹ BSA in PBS buffer (8.1 mM disodium phosphate, 1.9 mM sodium phosphate and 100 mM NaCl) at pH 7.4 with a flow rate of 20 µl·min⁻¹, 10 min adsorption time.(a) SPR sensogram of BSA adsorption onto regenerated blend films cellulose : HPCE DS 3 in different ratios. Measured with 785 nm laser. (b) According adsorbed dry mass of BSA, calculated with DeFeijter equation.

BSA adsorption on pure cellulose films was determined as 0.07 ± 0.04 mg·m^{-2} at pH 7.4, which is in good correlation with literature. [96] At pH 7.4, BSA and the cellulose are negatively charged. The replacement of the water molecules due to solvation on the surface is not very prone and there for nonspecific binding of BSA is not very likely. [97] Vice versa the nonpolar surface of the HPCE films is better accessible and at pH 7.4 and a BSA concentration of 1 mg·ml^{-1} solution 1.00 ± 0.07 mg·m^{-2} BSA was found to adsorb onto the surface. Adsorption to CSE, also a hairy rod derivative of cellulose with stearate substitutes, is reported in literature. Using also 1 mg·ml^{-1} BSA as adsorbate, 0.8 ± 0.1 mg·m^{-2} where found to remain after washing on the neat CSE surface also with 10 min injection time. In both cases hydrophobic C 18 chains promote non specific protein adsorption of BSA.

The adsorption of BSA occurs on all thin films very fast, noticeable through the steep slope in the sensogram, in the beginning of the adsorption step, and merges in a

plateau till the washing process. The adsorption amount does not correlate with the volume ratio used for spin coating. There is a minimum in the 1:1 ratio, which also exhibits when aligning the adsorption data with the effective surface ratio from AFM analyzation. (see Figure 40 a). The mixing ratios of 3:1 and 1:3 resulting in effective cellulose ratio of 0.57 and 0.31 do correlate to the linear trend between the adsorption on the neat films. Bringing the adsorbed mass in context with the surface free energy of the films, wettability seemed to be a curtail factor the BSA adsorption rather than the surface ratio of each phase. (see Figure 40 b)

5.7.2. QCM-D measurements

The gravimetrically measurement method QCM-D yields the mass of the system including water and incorporated electrolyte. Therefore, the viscoelastic properties of the films can be determined in principle. Together with the dry mass obtained by SPR measurement a comprehensive assessment of the thin films is possible.

BSA adsorption on regenerated Cellulose : HPCE DS 3 films

Before the BSA adsorption was implemented the films were equilibrated to PBS buffer. The frequency shift for the fifth overtone of each blend ratio is plotted in Figure 37 (a) with according dissipation in (b). The adsorption of wet BSA mass was calculated from the 5th overtone (f_5) and lined up with Johannsmann evaluation, which was determined from using overtone 5-11, density 1145 kg·m^{-3} and shear modulus of $7 \cdot 10^5$ Pa. The resulting effective mass is calculated, by elimination of mechanical stiffness, through the linear relation of $\Delta f/f$ over n^2.[81] (see Figure 38) 3.10

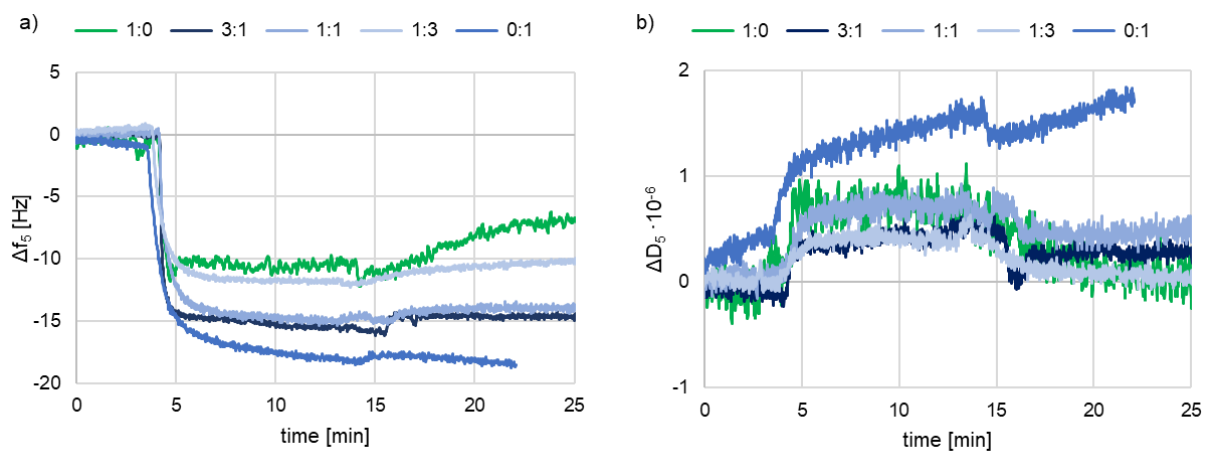*Figure 37 BSA adsorption at pH 7.4 on equilibrated cellulose : HPCE DS 3 surfaces of 1 mg·ml^{-1} BSA in PBS buffer (8.1 mM disodium phosphate, 1.9 mM sodium phosphate and 100 mM NaCl) at pH 7.4 with a flow rate of 0.1 ml·min^{-1}, 10 min adsorption time. Frequency shift in fifth overtone Δf_5 (a) and dissipation ΔD_5 respectively.*
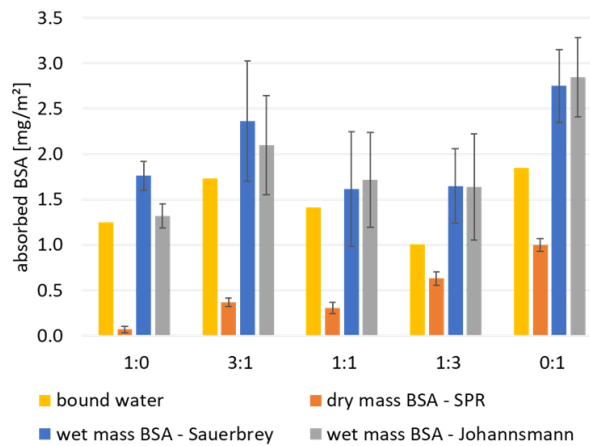
Figure 38 Results BSA adsorption by QCM: (blue) wet mass by Sauerbrey equation, (grey) Johannsmann evaluation in context with dry mass from SPR measurements (orange), using the complementary information of dry and wet mass the amount of bound water in BSA layer was calculated (yellow)

The calculations with the Sauerbrey equation were in good accordance with the Johannsmann evaluation, for adsorbing layer with very small dissipation (ΔD_5 0 – $0.5 \cdot 10^{-6}$) On neat HPCE DS 3 film most BSA adsorbed and it showed the largest dissipation ΔD_5 $1.7 \cdot 10^{-6}$. A wet mass of 2.8 ± 0.4 mg·m^{-2} was calculated. For the blend with 1:3 ratio 1.6 ± 0.5 mg·m^{-2} wet BSA was estimated with no dissipation. The dissipation for 1:1 was ΔD_5 $0.5 \cdot 10^{-6}$ and 1.7 ± 0.6 mg·m^{-2} wet BSA and for 3:1 ratio ΔD_5 $0.5 \cdot 10^{-6}$ with 2.1 ± 0.6 mg·m^{-2}

By using the complementary information of SPR measurement, which results in the dry mass, it is possible to calculate the bound water in the BSA using equation (10) (see Figure 39). Since on cellulose a small amount of dry mass (0.07 ± 0.04 mg·m^{-2}) was determined by SPR spectroscopy, this means that 95% of the detected mass by QCM is affiliated to bound water. BSA is known to form hydrogels at pH 7.4, due to cross linkage via intramolecular sulfide bridges of cysteine. [98] With rising content of the hydrophobic HPCE DS 3 phase the thin films are swelling less and the adsorbed BSA layer is getting more dense with less coupled water.
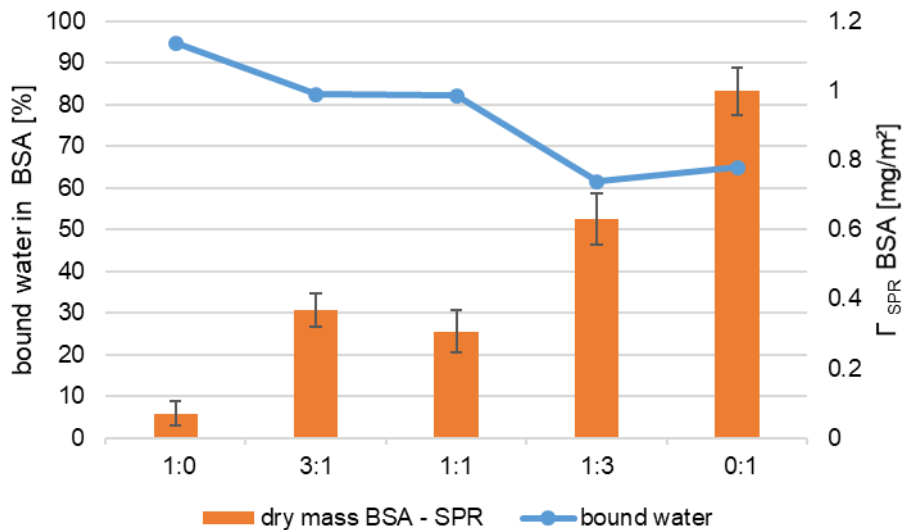
Figure 39 Water content [%] of the BSA layer on the cellulose : HPCE DS 3 blends compared to the adsorbed dry mass [mg·m⁻²]

When the results of the comprehensive BSA adsorption analysis with QCM-D and SPR are plotted against effective surface fraction (from the AFM analysis see chapter 5.5.1) and the surface free energy (SFE) (see chapter 5.4), it is noticeable, that the SPR data is close to the linear correlation between both pure films, while QCM-d data is not. The quantity of nonspecific protein adsorption is expected to arise with the increasing hydrophobic surface fraction, which is represented in a lower SFE value. Anyhow, the effective surface fraction is not in linear correlation with the SFE (see Figure 31). The 1:1 ratio, which was estimated with a surface fraction of 37% cellulose, was found with a surprisingly high SFE of 60.3 ± 0.6 mJ·m^{-2} and further resulted in lower BSA adsorption amount. Therefore, the surface fractions seem not to be the determining factor, but the wettability, which is affected by the morphology caused by the phase separation behavior.

Figure 40 From [85]: adsorbed BSA mass as function of the effective surface fraction (a) and of the surface free energy (b) dry mass from SPR measurements (blue triangle), wet mass from QCM-d measurements (red dots) and according bound water in BSA (black squares).

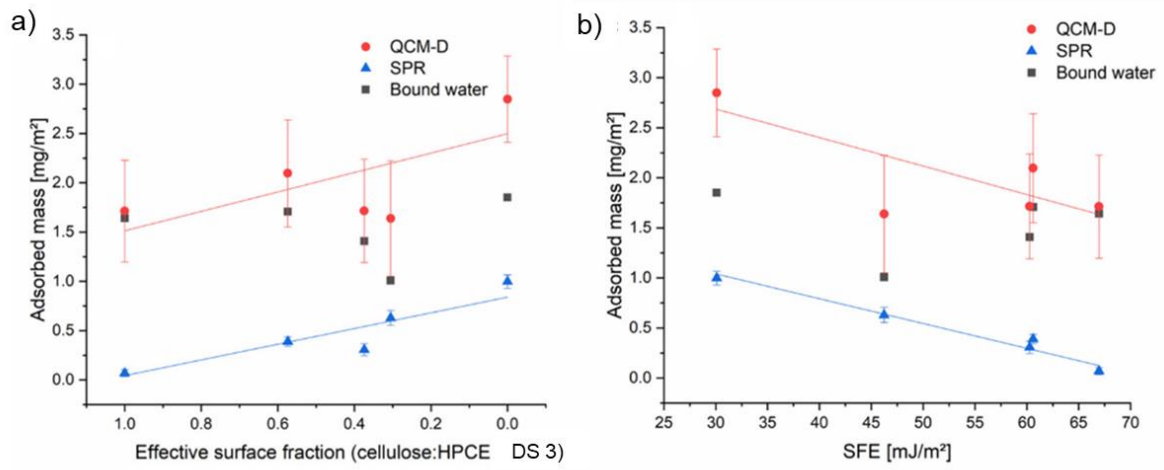*Water content in regenerated Cellulose : HPCE DS 3 films*

Using the difference in density of water and its deuterated derivative D_2O, it is possible to estimate the mass of exchangeable water within the thin films. The approach was first to estimate the water content of the different blend thin films and afterwards the films with adsorbed BSA layer on it. According curves are plotted in Figure 41.
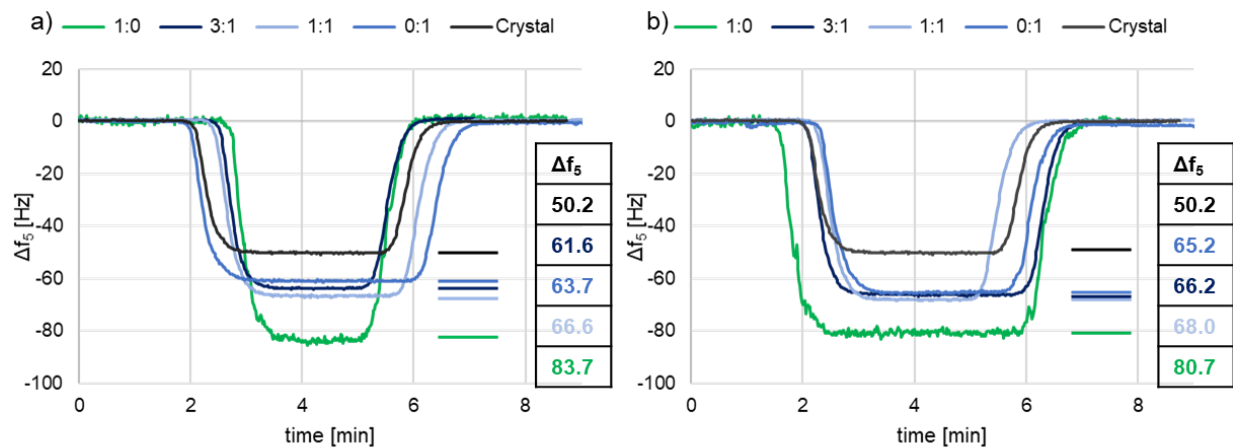
Figure 41 QCM graphs of water exchange experiments before (a) and after (b) BSA adsorption on blend system TMSC : HPCE DS 3.

According to Kittle et al. (2011) the water amount was calculated using the frequency shift of the pure crystal and the film, respectively f_5 [82]. The water amount was put in relation into the film mass calculated form the profilometer data, using the density value from literature for amorphous cellulose thin films 1145 kg·m^{-3}. [90,99]
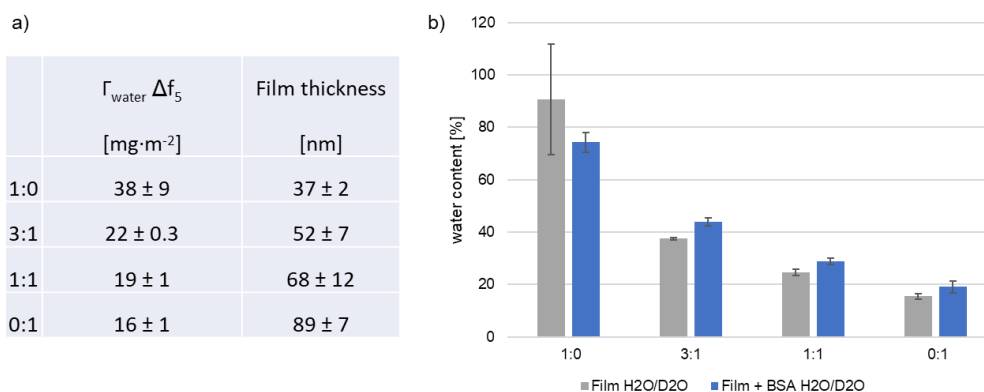
Figure 42 Calculated water amount in blend films and film thickness determined by profilometer (a) water content in % according to the film mass calculated using density of 1145 kg·m^{-3}

Neat cellulose films were estimated with a water content of 95 ± 21 %. In literature a water uptake is reported for amorphous cellulose films of 84 – 89 % [18] After BSA adsorption the water capability decreased to 74 ± 4 %. The neat HPCE DS 3 film was

estimated to have a 15 ± 1% water exchangeable. The blend films water exchangeability decreases with increasing amount of HPCE DS 3. After BSA adsorption the layer system of 3:1, 1:1 and neat HPCE DS 3 was able to exchange ~ 4-6% more water. This phenomenon was not observed for the cellulose film.

6. Conclusion and Outlook

Comprehensive surface studies on the blend systems TMSC : HPCE DS 3 and their according regenerated thin films were performed successfully. Including topography analysis and interaction behaviors with BSA at pH 7.4. The topography and the underlying microphase separation behavior were compared with the blend system with the HPCE derivative of DS 1. Non-contact AFM determinations visualized the coarsened phase separation pattern with HPCE DS 3, with feature sizes from 500 – 1500 nm in a thin film thickness of 100 – 130 nm. In contrast the polymer enhanced domains with the DS 1 derivative were much smaller and obeyed periodicity (200 – 1000 nm) at comparable film thickness.

The TMSC regeneration step was verified by ATR-IR and lead to film shrinkage, due to removal of the bulky trimethylsilyl group of the TMSC phase and inverted the phase separated height pattern. Further the water wettability as well as the SFE was increased.

Surprisingly the BSA adsorption could not be correlated with HPCE DS 3 phase ratio in the surface area. Instead it was rather found to be a function of the surface free energy hence nonspecific protein adsorption seems to be most influenced by wettability. The water content was found to be 95% for neat cellulose and 15% for neat HPCE DS 3.

Following the results in the present master thesis, FFM analysis were implemented on the TMSC : HPCE DS 3 blend system by Caterina Czibula at the Montanuniversity, Leoben. Based on recently reported unexpected tribological synergy in polyisoprene and polystyrene blend coatings a non-linear correlation of surface friction with the mixing ratio was expected. [100] BSA adsorption could not verified as a function of surface friction. [85]

7. Appendix

7.1. Acronyms

°	degree
°C	degree Celsius
µl	microliter
µm	micrometer
Å	Ångstroem
AFM	atomic force microscopy
ATR	attenuated total reflection
Au	gold
BSA	bovine serum albumin
C	-0.177 mg·m^{-2}·Hz^{-1} Sauerbrey constant
CA	contact angle
CHCl$_3$	chloroform
cm	centimeter
CMC	carboxymethyl cellulose
CTA	cellulose triacetate
D$_2$O	deuterium
DIM	diiodomethane
DMAc-LiCl	dimethylacetamide lithium chloride
dn/dc	refractive index increment
dn/dλ	chromatic dispersion
DNA	deoxyribonucleic acid
DS	degree of substitution
EC	ethyl cellulose
e.g.	example given
fps	frames per second
h	hour
H$_2$O	water
H$_2$O$_2$	hydrogen peroxide
HCl	hydrochloric acid
HPC	hydroxypropyl cellulose
HPCE	hydroxypropyl stearate cellulose
Hz	Hertz [sec^{-1}]
IR	infrared spectroscopy
k * d$_p$	constant
LB	Langmuir Blodgett (deposited films)
LiCl	ionic liquid lithium chloride
m	meter
Me	methyl group
MEK	methyl ethyl ketone
m$_f$	mass per unit area
mg	milligram
mg·m^{-2}	milligram per square meter

MilliQ	ultra-pure water 18.2 MΩ·cm^{-1} at RT
min	minute
mJ·m^{-2}	millijoule per square meter
ml	milliliter
mM	milli mole per liter
M$_n$	number average molar mass
M$_w$	molecular weight
n	refractive index
N$_2$	nitrogen (gaseous)
n$_a$, n$_b$	molar volume of the polymers
NaCl	natrium chloride
nm	nanometer
NMR	Nuclear magnetic resonance
ODM	organic monolayer
OWRK	Owen-Wendt-Rabel-Kaelble, method for estimation of SFE
PBS	phosphate buffer system with 8.1 mM disodium phosphate, 1.9 mM sodium phosphate and 100 mM NaCl at pH 7.4
PDI	polydisperse index
pH	negative decimal logarithmic of acid concentration
PHB	poly-3-hydroxybutyrate
pI	isoelectric point
pK$_a$	acid dissociation constant
PMMA	polymethylmethacrylate
PS	polystyrene
PVDF	polyvinylidene fluoride
QCM-D	quartz crystal microbalance with dissipation monitoring
R	gas constant 8.3145·K^{-1}·mol^{-1}
reg	regeneration procedure (exposure to HCl vapor)
RMS	root mean square value
rpm	revolutions per minute
RT	room temperature
s	second
SFE	Surface free energy
Si	Silicon
SPR	surface plasmon resonance spectroscopy
sym.	symmetrical
T	temperature
THF	tetrahydrofuran
TIR	total internal reflection
TMSC	Trimethylsilyl Cellulose
TU	technical university
US	ultra-sonic
vol%	volume percentage
w%	weight percentage
Γ_{water}	mass auf exchanged water

ΔD	change in dissipation
Δf_n	change in frequency (n … number of overtone)
ΔG_{mix},	change in gibbs free enthalpy
ΔH_{mix}	change in enthalpy of mixing
ΔS_{mix}	change in entropy of mixing
θ	contact angle
θ_1	angle of incident beam
θ_2	angle of outgoing beam
ρ	density
ρ_{D2O}	1.1050 g*cm^{-3} at 20°C
ρ_{H2O}	0.9982 g*cm^{-3} at 20°C
σ	sigma root mean square (RMS) value of the height irregularities [nm]
σ_l^D	disperse ratio of interfacial tension between solid and liquid
σ_{lg}	interfacial tension between liquid and gas
σ_l^P	polar ratio of interfacial tension between solid and liquid
σ_{ls}	interfacial tension between solid and liquid
σ_s^D	disperse ratio of interfacial tension between solid and liquid
σ_{sg}	interfacial tension between solid and gas
σ_s^P	polar ratio of interfacial tension between solid and liquid
Φ_a, Φ_b	volume fraction
χ	flory huggins interaction
$(\frac{\Delta f_n}{n})_{film}$	shift in frequency due to D$_2$O exchange in film
$(\frac{\Delta f_n}{n})_{bare}$	shift in frequency due to D$_2$O exchange on bare crystal

7.2. References

[1] K. Jin, Z. Qin, M.J. Buehler, Molecular deformation mechanisms of the wood cell wall material, *Journal of the mechanical behavior of biomedical materials* 42 **(2015)** 198–206.

[2] R.J. Moon, A. Martini, J. Nairn, J. Simonsen, J. Youngblood, Cellulose nanomaterials review, *Chemical Society reviews* 40 **(2011)** 3941–3994.

[3] J. Credou, T. Berthelot, Cellulose: from biocompatible to bioactive material, *Journal of Materials Chemistry B* 2 **(2014)** 4767–4788.

[4] D. Klemm, Comprehensive Cellulose Chemistry, Volume 1: Fundamentals and Analytical Methods, 1st ed., Weinheim, 1998.

[5] A.C. O'Sullivan, Cellulose: the structure slowly unravels, *Cellulose* 4 **(1997)** 173–207.

[6] M. Müller, C. Czihak, H. Schober, Y. Nishiyama, G. Vogl, All Disordered Regions of Native Cellulose Show Common Low-Frequency Dynamics, *Macromolecules* 33 **(2000)** 1834–1840.

[7] J. Demeter, W. Mormann, J. Schmidt, W. Burchard, Solution Behavior of Trimethylsilyl Cellulose of Different Degrees of Substitution, Studied by Static and Dynamic Light Scattering, *Macromolecules* 36 **(2003)** 5297–5303.

[8] K. Petzold, A. Koschella, D. Klemm, B. Heublein, Silylation of Cellulose and Starch – Selectivity, Structure Analysis, and Subsequent Reactions, *Cellulose* 10 **(2003)** 251–269.

[9] L. Nyfors, M. Suchy, J. Laine, E. Kontturi, Ultrathin cellulose films of tunable nanostructured morphology with a hydrophobic component, *Biomacromolecules* 10 **(2009)** 1276–1281.

[10] E. Kontturi, P.C. Thüne, J.W. Niemantsverdriet, Cellulose Model Surfaces - Simplified Preparation by Spin Coating and Characterization by X-ray Photoelectron Spectroscopy, Infrared Spectroscopy, and Atomic Force Microscopy, *Langmuir* 19 **(2003)** 5735–5741.

[11] S. Strasser, K. Niegelhell, M. Kaschowitz, S. Markus, R. Kargl, K. Stana-Kleinschek, C. Slugovc, T. Mohan, S. Spirk, Exploring Nonspecific Protein Adsorption on Lignocellulosic Amphiphilic Bicomponent Films, *Biomacromolecules* 17 **(2016)** 1083–1092.

[12] K. Niegelhell, M. Süßenbacher, K. Jammernegg, T. Ganner, D. Schwendenwein, H. Schwab, F. Stelzer, H. Plank, S. Spirk, Enzymes as Biodevelopers for Nano-

And Micropatterned Bicomponent Biopolymer Thin Films, *Biomacromolecules* 17 **(2016)** 3743–3749.

[13] K. Niegelhell, M. Süßenbacher, J. Sattelkow, H. Plank, Y. Wang, K. Zhang, S. Spirk, How Bound and Free Fatty Acids in Cellulose Films Impact Nonspecific Protein Adsorption, *Biomacromolecules* 18 **(2017)** 4224–4231.

[14] M. Schaub, G. Wenz, G. Wegner, A. Stein, D. Klemm, Ultrathin films of cellulose on silicon wafers, *Advanced Materials* 5 **(1993)** 919–922.

[15] E. Kontturi, T. Tammelin, M. Osterberg, Cellulose--model films and the fundamental approach, *Chemical Society reviews* 35 **(2006)** 1287–1304.

[16] T. Ganner, J. Sattelkow, B. Rumpf, M. Eibinger, D. Reishofer, R. Winkler, B. Nidetzky, S. Spirk, H. Plank, Direct-Write Fabrication of Cellulose Nano-Structures via Focused Electron Beam Induced Nanosynthesis, *Scientific reports* 6 **(2016)** 32451.

[17] A. Wolfberger, A. Petritz, A. Fian, J. Herka, V. Schmidt, B. Stadlober, R. Kargl, S. Spirk, T. Griesser, Photolithographic patterning of cellulose: a versatile dual-tone photoresist for advanced applications, *Cellulose* 22 **(2015)** 717–727.

[18] E. Kontturi, M. Suchy, P. Penttilä, B. Jean, K. Pirkkalainen, M. Torkkeli, R. Serimaa, Amorphous Characteristics of an Ultrathin Cellulose Film, *Biomacromolecules* 12 **(2011)** 770–777.

[19] M. Nau, D. Seelinger, M. Biesalski, Functional surface coatings from tailor-made long-chain hydroxypropyl cellulose ester nanoparticles, *Cellulose* 25 **(2018)** 5769–5780.

[20] H. Hou, A. Reuning, J.H. Wendorff, A. Greiner, Effect of Blending of Cholesteric Cellulose Esters on the Pitch Height, *Macromolecular bioscience* 1 **(2001)** 45–48.

[21] E. Kontturi, S. Spirk, Ultrathin Films of Cellulose: A Materials Perspective, *Frontiers in Chemistry* 7 **(2019)** 488.

[22] D.B. Hall, P. Underhill, J.M. Torkelson, Spin coating of thin and ultrathin polymer films, *Polymer Engineering & Science* 38 **(1998)** 2039–2045.

[23] S. Walheim, M. Böltau, J. Mlynek, G. Krausch, U. Steiner, Structure Formation via Polymer Demixing in Spin-Cast Films, *Macromolecules* 30 **(1997)** 4995–5003.

[24] E. Kontturi, P. Laaksonen, M.B. Linder, Nonappa, A.H. Gröschel, O.J. Rojas, O. Ikkala, Advanced Materials through Assembly of Nanocelluloses, *Advanced Materials* 30 **(2018)** e1703779.

[25] M. Weißl, M.A. Hobisch, L.S. Johansson, K. Hettrich, E. Kontturi, B. Volkert, S. Spirk, Cellulose carbamate derived cellulose thin films: preparation, characterization and blending with cellulose xanthate, *Cellulose* 26 **(2019)** 7399–7410.

[26] M. Weißl, K. Niegelhell, D. Reishofer, A. Zankel, J. Innerlohinger, S. Spirk, Homogeneous cellulose thin films by regeneration of cellulose xanthate: properties and characterization, *Cellulose* 25 **(2018)** 711–721.

[27] J. Schurz, Physikalische Chemie der Hochpolymeren: Eine Einführung, Springer, Berlin, Heidelberg, 1974.

[28] B.A. Miller-Chou, J.L. Koenig, A review of polymer dissolution, *Progress in Polymer Science* 28 **(2003)** 1223–1270.

[29] S. Gårdebjer, M. Andersson, J. Engström, P. Restorp, M. Persson, A. Larsson, Using Hansen solubility parameters to predict the dispersion of nano-particles in polymeric films, *Polymer Chemistry* 7 **(2016)** 1756–1764.

[30] J. Koo, S. Satija, J.-S. Lee, Y.-S. Seo, Spontaneous bilayer phase separations of spin-coated polymer blend thin films: A neutron reflectivity study, *Macromolecular Research* 24 **(2016)** 1105–1110.

[31] S.Y. Heriot, R.A.L. Jones, An interfacial instability in a transient wetting layer leads to lateral phase separation in thin spin-cast polymer-blend films, *Nature materials* 4 **(2005)** 782–786.

[32] Reiter, Dewetting of thin polymer films, *Physical review letters* 68 **(1992)** 75–78.

[33] A.M.J. Edwards, R. Ledesma-Aguilar, M.I. Newton, C.V. Brown, G. McHale, Not spreading in reverse: The dewetting of a liquid film into a single drop, *Science advances* 2 **(2016)** e1600183.

[34] F.B. Wyart, P. Martin, C. Redon, Liquid/liquid dewetting, *Langmuir* 9 **(1993)** 3682–3690.

[35] C. Sagui, M. Grant, Theory of nucleation and growth during phase separation, *Physical Review E* 59 **(1999)** 4175–4187.

[36] K. Tanaka, A. Takahara, T. Kajiyama, Film Thickness Dependence of the Surface Structure of Immiscible Polystyrene/Poly(methyl methacrylate) Blends, *Macromolecules* 29 **(1996)** 3232–3239.

[37] S. Roy, A. Sharma, Self-organized morphological evolution and dewetting in solvent vapor annealing of spin coated polymer blend nanostructures, *Journal of Colloid and Interface Science* 449 **(2015)** 215–225.

[38] L. Taajamaa, O.J. Rojas, J. Laine, E. Kontturi, Phase-specific pore growth in ultrathin bicomponent films from cellulose-based polysaccharides, *Soft Matter* 7 **(2011)** 10386–10394.

[39] E. Kontturi, L.-S. Johansson, J. Laine, Cellulose decorated cavities on ultrathin films of PMMA, *Soft Matter* 5 **(2009)** 1786–1788.

[40] E. Kontturi, L. Nyfors, J. Laine, Utilizing Polymer Blends to Prepare Ultrathin Films with Diverse Cellulose Textures, *Macromolecular Symposia* 294 **(2010)** 45–50.

[41] E. Kontturi, P.C. Thüne, J.W. Niemantsverdriet, Trimethylsilylcellulose/Polystyrene Blends as a Means To Construct Cellulose Domains on Cellulose, *Macromolecules* 38 **(2005)** 10712–10720.

[42] G. Hu, J.A. Heitmann, O.J. Rojas, In situ monitoring of cellulase activity by microgravimetry with a quartz crystal microbalance, *The journal of physical chemistry. B* 113 **(2009)** 14761–14768.

[43] E. Meyer, H.J. Hug, R. Bennewitz, Scanning Probe Microscopy: The Lab on a Tip, Springer, Berlin, Heidelberg, 2004.

[44] K.D. Jandt, Atomic force microscopy of biomaterials surfaces and interfaces, *Surface Science* 491 **(2001)** 303–332.

[45] How does atomic force microscopy work? - Quora, https://www.quora.com/How-does-atomic-force-microscopy-work#InbII (accessed 9.06.2019).

[46] U. Maver, T. Maver, Z. Persin, M. Mozetic, A. Vesel, M. Gaberscek, K. Stana-Kleinschek, Polymer Characterization with the Atomic Force Microscope, in: H.B. Yamak (Ed.), Emulsion Polymerization: Effects of Polymerization Variables on the Properties of Vinyl Acetate Based Emulsion Polymers, INTECH Open Access Publisher, 2013.

[47] R. García, R. Pérez, Dynamic atomic force microscopy methods, *Surface Science Reports* 47 **(2002)** 197–301.

[48] S. Pawlizak, J. Gerdelmann, C. Brunner, Introduction: Scanning Force Microscopy (SFM) - Soft Matter Physics Division - University of Leipzig, http://home.uni-leipzig.de/pwm/web/?section=introduction&page=sfm (accessed 12.06.2019).

[49] P. Klapetek, Quantitative data processing in scanning probe microscopy: SPM applications for nanometrology, Elsevier, Amsterdam, Netherlands, 2018.

[50] M. Rabe, D. Verdes, S. Seeger, Understanding protein adsorption phenomena at solid surfaces, *Advances in colloid and interface science* 162 **(2011)** 87–106.

[51] D.L. Nelson, M.M. Cox, A.L. Lehninger, B. Häcker, Lehninger Biochemie: Mit 131 Tabellen, 4th ed., Springer, Berlin, 2009.

[52] R.A. Latour, Biomaterials: Protein-Surface Interactions, in: G.E. Wnek, G.I. Bowin (Eds.), Encyclopedia of Biomaterials and Biomedical Engineering, Taylor & Francis, 2005, pp. 270–278.

[53] B.X. Huang, H.-Y. Kim, C. Dass, Probing three-dimensional structure of bovine serum albumin by chemical cross-linking and mass spectrometry, *Journal of the American Society for Mass Spectrometry* 15 **(2004)** 1237–1247.

[54] J.E. Kinsella, D.M. Whitehead, Proteins in whey: chemical, physical, and functional properties, *Advances in food and nutrition research* 33 **(1989)** 343–438.

[55] D.R. Schmidt, H. Waldeck, J.K. Weiyan, Protein Adsorption to Biomaterials, in: D.A. Puleo, R. Bizios (Eds.), Biological interactions on materials surfaces: Understanding and controlling protein, cell, and tissue responses, Springer, New York, 2009.

[56] NicoyaLifesciences, 4 Ways to Reduce Non-Specific Binding in SPR Experiments, https://nicoyalife.com/blog/4-ways-reduce-non-specific-binding-spr/, 2015 (accessed 21.05.2019).

[57] K. Takeda, A. Wada, K. Yamamoto, Y. Moriyama, K. Aoki, Conformational change of bovine serum albumin by heat treatment, *Journal of protein chemistry* 8 **(1989)** 653–659.

[58] K.C. Dee, D.A. Puleo, R. Bizios, An introduction to tissue-biomaterial interactions, Wiley-Liss, Hoboken, NJ, 2002.

[59] T. Mohan, K. Niegelhell, C.S.P. Zarth, R. Kargl, S. Köstler, V. Ribitsch, T. Heinze, S. Spirk, K. Stana-Kleinschek, Triggering protein adsorption on tailored cationic cellulose surfaces, *Biomacromolecules* 15 **(2014)** 3931–3941.

[60] P.G. Squire, P. Moser, C.T. O'Konski, Hydrodynamic properties of bovine serum albumin monomer and dimer, *Biochemistry* 7 **(1968)** 4261–4272.

[61] P. Moser, P.G. Squire, C.T. O'Konski, Electric Polarization in Proteins—Dielectric Dispersion and Kerr Effect Studies of Isoionic Bovine Serum Albumin 1, *The Journal of Physical Chemistry* 70 **(1966)** 744–756.

[62] W. Norde, C.E. Giacomelli, BSA structural changes during homomolecular exchange between the adsorbed and the dissolved states, *Journal of Biotechnology* 79 **(2000)** 259–268.

[63] D.A. Puleo, R. Bizios (Eds.), Biological interactions on materials surfaces: Understanding and controlling protein, cell, and tissue responses, Springer, New York, 2009.

[64] W. Norde, J. Lyklema, Why proteins prefer interfaces, *Journal of Biomaterials Science, Polymer Edition* 2 **(1991)** 183–202.

[65] T. Wangkam, S. Yodmongkol, J. Disrattakit, B. Sutapun, R. Amarit, A. Somboonkaew, T. Srikhirin, Adsorption of bovine serum albumin (BSA) on polystyrene (PS) and its acid copolymer, *Current Applied Physics* 12 **(2012)** 44–52.

[66] I. Reviakine, D. Johannsmann, R.P. Richter, Hearing what you cannot see and visualizing what you hear, *Analytical chemistry* 83 **(2011)** 8838–8848.

[67] J.A. de Feijter, J. Benjamins, F.A. Veer, Ellipsometry as a tool to study the adsorption behavior of synthetic and biopolymers at the air-water interface, *Biopolymers* 17 **(1978)** 1759–1772.

[68] N.J. de Mol, M.J.E. Fischer, Surface Plasmon Resonance: Methods and Protocols, 1st ed., Humana Press, Totowa, NJ, 2010.

[69] H.R. Gwon, S.H. Lee, Spectral and Angular Responses of Surface Plasmon Resonance Based on the Kretschmann Prism Configuration, *Materials Transactions* 51 **(2010)** 1150–1155.

[70] BioNavis: How does MP-SPR work?, http://www.bionavis.com/en/life-science/technology/ (accessed 18.08.2019).

[71] R.B.M. Schasfoort (Ed.), Handbook of Surface Plasmon Resonance, Royal Society of Chemistry, Cambridge, 2017.

[72] O.K. Kari, T. Rojalin, S. Salmaso, M. Barattin, H. Jarva, S. Meri, M. Yliperttula, T. Viitala, A. Urtti, Multi-parametric surface plasmon resonance platform for studying liposome-serum interactions and protein corona formation, *Drug Delivery and Translational Research* 7 **(2017)** 228–240.

[73] J.A. Marquart, SPR Theory, https://www.sprpages.nl/spr-overview/spr-theory, 2019 (accessed 24.06.2019).

[74] C. Sampl, K. Niegelhell, D. Reishofer, R. Resel, S. Spirk, U. Hirn, Multilayer Density Analysis of Cellulose Thin Films, *Frontiers in Chemistry* 7 **(2019)** 251.

[75] K.A. Peterlinz, R. Georgiadis, Two-color approach for determination of thickness and dielectric constant of thin films using surface plasmon resonance spectroscopy, *Optics Communications* 130 **(1996)** 260–266.

[76] T. Tammelin, R. Abburi, M. Gestranius, C. Laine, H. Setälä, M. Österberg, Correlation between cellulose thin film supramolecular structures and interactions with water, *Soft Matter* 11 **(2015)** 4273–4282.

[77] G. Sauerbrey, Verwendung von Schwingquarzen zur Wägung dünner Schichten und zur Mikrowägung, *Zeitschrift für Physik* 155 **(1959)** 206–222.

[78] A.W. Warner, C. d. Stockbridge, Quartz Resonators; Reduction of Transient Frequency Excursion Due to Temperature Change, *Journal of Applied Physics* 34 **(1963)** 437–438.

[79] Nanoscience-Instruments, Quartz Crystal Microbalance (QCM) - Nanoscience Instruments, https://www.nanoscience.com/techniques/quartz-crystal-microbalance/#energydissipation (accessed 13.03.2019).

[80] M.V. Voinova, M. Rodahl, M. Jonson, B. Kasemo, Viscoelastic Acoustic Response of Layered Polymer Films at Fluid-Solid Interfaces: Continuum Mechanics Approach, *Physica Scripta* 59 **(1999)** 391–396.

[81] D. Johannsmann, Derivation of the shear compliance of thin films on quartz resonators from comparison of the frequency shifts on different harmonics, *Journal of Applied Physics* 89 **(2001)** 6356–6364.

[82] J.D. Kittle, X. Du, F. Jiang, C. Qian, T. Heinze, M. Roman, A.R. Esker, Equilibrium water contents of cellulose films determined via solvent exchange and quartz crystal microbalance with dissipation monitoring, *Biomacromolecules* 12 **(2011)** 2881–2887.

[83] T. Mohan, S. Spirk, R. Kargl, A. Doliška, A. Vesel, I. Salzmann, R. Resel, V. Ribitsch, K. Stana-Kleinschek, Exploring the rearrangement of amorphous cellulose model thin films upon heat treatment, *Soft Matter* 8 **(2012)** 9807–9815.

[84] D.K. Owens, R.C. Wendt, Estimation of the surface free energy of polymers, *Journal of Applied Polymer Science* 13 **(1969)** 1741–1747.

[85] C. Czibula, G. Teichert, M. Nau, M. Hobisch, C. Palasingh, M. Biesalski, S. Spirk, C. Teichert, T. Nypelö, Design of Friction, Morphology, Wetting, and Protein Affinity by Cellulose Blend Thin Film Composition, *Frontiers in Chemistry* 7 **(2019)** 338.

[86] D. Nečas, P. Klapetek, Gwyddion: an open-source software for SPM data analysis, *Open Physics* 10 **(2011)** 181–188.

[87] P. Klapetek, D. Nečas, C. Anderson, Gwyddion user guide, http://gwyddion.net/documentation/user-guide-en/, 2019 (accessed 28.08.2019).

[88] J.L. Robeson, R. d. Tilton, Spontaneous Reconfiguration of Adsorbed Lysozyme Layers Observed by Total Internal Reflection Fluorescence with a pH-Sensitive Fluorophore, *Langmuir* 12 **(1996)** 6104–6113.

[89] H. Zhao, P.H. Brown, P. Schuck, On the distribution of protein refractive index increments, *Biophysical journal* 100 **(2011)** 2309–2317.

[90] T. Mohan, K. Niegelhell, C. Nagaraj, D. Reishofer, S. Spirk, A. Olschewski, K. Stana Kleinschek, R. Kargl, Interaction of Tissue Engineering Substrates with Serum Proteins and Its Influence on Human Primary Endothelial Cells, *Biomacromolecules* 18 **(2017)** 413–421.

[91] T. Mohan, R. Kargl, A. Doliška, A. Vesel, S. Köstler, V. Ribitsch, K. Stana-Kleinschek, Wettability and surface composition of partly and fully regenerated cellulose thin films from trimethylsilyl cellulose, *Journal of Colloid and Interface Science* 358 **(2011)** 604–610.

[92] P. Wang, Koberstein j. T., Morphology of Immiscible Polymer Blend Thin Films Prepared by Spin-Coating, *Macromolecules* 37 **(2004)** 5671–5681.

[93] P.E.R. Durigon, D.F.S. Petri, H. Drings, T. Schimmel, M. Bruns, Characterization and modification of polymer blend films, *Colloid & Polymer Science* 279 **(2001)** 1013–1019.

[94] G. Bar, L. Delineau, R. Brandsch, M. Bruch, M.-H. Whangbo, Importance of the indentation depth in tapping-mode atomic force microscopy study of compliant materials, *Applied Physics Letters* 75 **(1999)** 4198–4200.

[95] C. Teichert, A. Haas, G.M. Wallner, R.W. Lang, Nanometer scale characterization of polymer films by atomic-force microscopy, *Macromolecular Symposia* 181 **(2002)** 457–466.

[96] K. Niegelhell, T. Ganner, H. Plank, E. Jantscher-Krenn, S. Spirk, Lectins at Interfaces-An Atomic Force Microscopy and Multi-Parameter-Surface Plasmon Resonance Study, *Materials* 11 **(2018)** 2348.

[97] H. Orelma, I. Filpponen, L.-S. Johansson, J. Laine, O.J. Rojas, Modification of cellulose films by adsorption of CMC and chitosan for controlled attachment of biomolecules, *Biomacromolecules* 12 **(2011)** 4311–4318.

[98] G. Navarra, C. Peres, M. Contardi, P. Picone, P.L. San Biagio, M. Di Carlo, D. Giacomazza, V. Militello, Heat- and pH-induced BSA conformational changes, hydrogel formation and application as 3D cell scaffold, *Archives of Biochemistry and Biophysics* 606 **(2016)** 134–142.

[99] R.A. Gross, B. Kalra, Biodegradable polymers for the environment, *Science* 297 **(2002)** 803–807.

[100] Jillian A. Emerson, Nikolay T. Garabedian, Axel C. Moore, David L. Burris, Eric M. Furst, Thomas H. Epps, III, Unexpected Tribological Synergy in Polymer Blend Coatings: Leveraging Phase Separation to Isolate Domain Size Effects and Reduce Friction, *ACS Applied Materials Interfaces* 9 **(2017)** 34480–34488.